Electronic Structure of Oxides and Perovskites: A Benchmark Database

Master's Thesis

submitted to

Indian Institute of Science Education and Research Tirupati

in partial fulfillment of the requirements for the

BS-MS Dual Degree Programme

by

Kshitij Sinha

Roll Number: 20191117

Supervisor: Prof. Dr. Claudia Draxl

Humboldt Universität zu Berlin

Berlin, Germany

April, 2024

Certificate

This is to certify that the MS Thesis entitled **Electronic Structure of Oxides and Perovskites: A Benchmark Database**, submitted towards the partial fulfilment of the BS-MS dual degree programme at the Indian Institute of Science Education and Research Tirupati, represents the study / work carried out by **Mr. Kshitij Sinha** at **Humboldt Universität zu Berlin, Berlin, Germany** under the supervision of **Prof. Dr. Claudia Draxl**, Department of **Physics**, during the academic year 2023-2024 and the same has not been submitted for any other degree or diploma of any other university or institute.

Name of student: Kshitij Sinha

Roll Number: 20191117

Signature of student:

Date : 31/03/2024

Name of Supervisor: Prof. Dr. Claudia Draxl

Signature of Supervisor: 

Date: 31/03/2024

Declaration

I declare that the matter presented in the MS thesis entitled **Electronic Structure of Oxides and Perovskites: A Benchmark Database**, are the results of the work carried out by me at the Department of **Physics, Humboldt Universität zu Berlin, Berlin, Germany**, under the supervision of **Prof. Dr. Claudia Draxl**.

I declare that the study / work submitted is my own and expressed in my own words.

. . . . . .

I confirm that appropriate credit has been given within this thesis where reference has been made to the work of others. I also declare that I have adhered to all principles of academic ethics and integrity and have not fabricated or falsified any idea / data / fact / image source in my submission.

I understand that violation of the above will lead to disciplinary action by the Institute and can also evoke penal action from the sources which have thus not been properly cited or from whom proper permission has not been obtained.

Name of student: Kshitij Sinha

Roll Number: 20191117

Signature of student:

Date : 31/03/2024

Endorsed by:

Name of Supervisor: Prof. Dr. Claudia Draxl

Signature of Supervisor: 

Date: 31/03/2024

Acknowledgements

Firstly, I express my deepest gratitude to my supervisor, Prof. Dr. Claudia Draxl, for offering me a project in her group. Her guidance, expertise, support and trust have been fundamental in shaping this project. I have gained huge insights into effective research methodologies and principles of physics through our valuable discussions.

Secondly, I thank Dr. Pasquale Pavone and Dr. Andris Gulans for their invaluable assistance, insightful discussions and feedback. I also thank Sven Lubeck, Cecilia Vona, Ignacio Gonzalez Oliva, Marti Raya Moreno and other group members for their prompt help whenever I encountered uncertainties or had questions.

I would also like to thank all the members of the SOL group for their warm welcome and rich discussions during coffee and lunch breaks. These discussions undoubtedly contributed to the development of this thesis. Furthermore, I thoroughly enjoyed my time in Berlin thanks to our fantastic after-work activities and dinners.

Additionally, I thank IISER Tirupati for allowing me to conduct a master's thesis project at a research group of choice. I firmly believe that this opportunity has been invaluable in providing exposure and gaining skills, making it undoubtedly the most significant highlight of our curriculum.

Lastly, I thank my friends and family for their constant love, encouragement, and understanding throughout this project.

Abstract

Both perovskites and oxide materials have gained significant attention in recent years due to their unique properties and, thus, a wide range of possible applications. In this work, we investigate from first principles metal-oxide and halide perovskites, like $BaSnO_3$, $CsPbI_3$, etc., and large band-gap oxide materials, like Ga_2O_3, ZrO_2, etc. We focus on their electronic properties, computing their electronic band structure and band gap, the density of states, effective masses, and more by applying density-functional theory. We employ a range of density functionals, i.e. the local density approximation (LDA), the generalized gradient approximation (PBEsol), as well as the hybrid functionals PBE0 and HSE06. All calculations are carried out with the full-potential all-electron package **exciting**, that implements the linearized augmented planewave plus local orbital (LAPW+lo) basis to achieve highly precise results. **exciting** exhibits thus proven benchmark quality, reaching μHa precision. Our calculations present benchmark calculations that can serve as valuable reference data for the community.

Keywords: DFT; Electronic Structure; Perovskites; Benchmarking

Contents

List of Figures

List of Tables

Chapter 1

Introduction

Electronic structure calculations are an essential facet of condensed matter physics, providing insights into the behaviour of electrons in a structure and offering valuable information about a material's properties. These calculations involve computational techniques to analyse the distribution of electrons within atoms, molecules or solids. For solids, the behaviour of electrons dictates various macroscopic physical properties, such as electrical and thermal conductivity, magnetism, and more. Therefore, understanding the electronic structure of such systems is crucial for developing materials with tailored functionalities.

Electronic structure calculations involve a range of theoretical methods, from *ab initio* approaches that solve the Schrödinger equation without empirical parameters, to semi-empirical methods that incorporate empirical data or approximations to describe electronic behavior, like the Tight Binding model [3]. Various *ab initio* and wave function-based methods, such as Hartree-Fock [4], Density-Functional Theory [5], are available. Density-functional theory (DFT) is a widely used and versatile method that balances computational efficiency and accuracy for various materials. DFT is heavily adopted by the scientific community, with more than 15,000 papers published each year, as per a study done in 2015 [6, 7]. This popularity has led to many individual theory implementations by research groups and commercial entities.

To perform a DFT calculation accurately, it is essential to model the system appropriately using input parameters such as lattice parameters, atomic coordinates, and boundary conditions. A DFT calculation requires a set of well-defined basis functions to model the Kohn-Sham wavefunctions. The precision of the calculation strongly depends on the basis set. In addition to the basis set, other parameters determine the sampling of the wavefunction. These parameters are method and code-specific, but in any case, having a set of well-converged parameters is essential for obtaining

satisfactory results.

While numerous computational databases are available online, which provide extensive electronic structure calculations publicly, these databases mainly contain calculations up to a certain level of precision [2, 8, 9, 10]. This is partly because researchers do not require theoretical simulations of the highest precision in practice and partly because inexpensive simulation methods such as DFT enable the community to perform cheap and satisfactory calculations conveniently. It is apparent that despite the crucial role it plays in materials design and discovery, there is a shortage of precise electronic structure calculations that can serve as reference points for data analysis or future computations.

Benchmark calculations are defined as computations that assess the accuracy of a particular method to the fullest extent possible. To achieve this, it is crucial to carefully set up the calculations by selecting parameters that reflect well-converged results. Convergence, in this context, refers to computing many calculations with varying input parameters until the error in an observable is minimized to a certain threshold. It is important to distinguish between accuracy and precision in calculations. 'Accuracy' refers to how close a value is to a well-established value, usually determined with a higher-level method or experimentally. 'Precision' refers to the consistency of results within a chosen framework. A value is considered more 'precise' if the deviation in successive values is minimal, usually quantified against a threshold [11].

This work aims to address the lack of highly precise electronic structure calculations in the community by performing benchmark quality calculations on perovskites and wide-bandgap oxide materials using **`exciting`**, an open-source DFT package [1]. Both sets of materials possess unique and profound properties, making them widely studied by the community for exploring applications. These computations are intended to serve as reference calculations for the community and are published on NOMAD, an online database with free public access [2]. We analyze various electronic properties, such as the electronic band structure and density of states, the bandgap, and effective masses.

Another issue when using DFT is the dilemma of choosing the appropriate density functional [12]. In this study, we evaluated six materials using a pool of four exchange-correlation functionals to compare the results. Since the focus is solely on obtaining the most precise results for each case, any comparison to experimental values is beyond the scope of this work.

Outline of the thesis:

Chapter 2 provides a comprehensive overview of perovskites and wide-bandgap oxide systems, discussing their historical development, significance, as well as their physical and chemical properties. The crystal structures of these systems is also described.

Chapter 3 establishes the theoretical framework used in this work, building upon the foundation laid in *Chapter 2*. The derivation of the modern Kohn-Sham DFT formalism will be presented, followed by a review of the implementation of the Linearized Augmented Planewaves (LAPW) + local orbital (lo) basis set. The advantages of this method in solving the KS-equations will be presented. Additionally, the various exchange-correlation functionals, their applications, differences, and implications for calculations will be discussed.

Chapter 4 provides the workflow for the computation and analysis performed in this work. It contains information about the computational framework and the steps followed in a general protocol. The chapter lists the key ingredients for increasing the precision of a calculation within the LAPW+lo method, with a very detailed example.

Chapter 5 presents the results of our calculations, with emphasis on the band properties. This is followed by a critical analysis of the results in *Chapter 6*. We discuss and draw inferences on the observed patterns within the scope of this work. *Chapter 7* summarizes the study with concluding remarks and presents future directions.

Chapter 2

Investigated Materials: Structure and Importance

2.1 Perovskites

Perovskites have garnered significant attention due to their unique physical properties, versatile behavior, and wide range of applications. The term perovskite was originally used to describe the oxide mineral $CaTiO_3$, but it has since evolved to represent a class of materials with a similar structure to $CaTiO_3$ [13]. Hence, perovskites are materials with a characteristic ABX_3 - type crystal structure, where A is typically an alkaline or rare earth metal surrounded by a transition metal cation B and the anions X.

Fig. (2.1) shows an example of the cubic perovskite $BaSnO_3$ with space group *Pm-3m*. The A cations reside in the corners of the cubic unit cell; the B cation is positioned in the centre with 6-fold coordination to the surrounding X anions, arranged in an octahedral geometry around it [14]. The X site is occupied by oxygen with an oxidation state of -1, resulting in [+3] total charge that is balanced by the $Ba^{[+1]}$ and $Sn^{[+2]}$ cations.

Goldschmidt estimated the ability of an ABX_3 - type compound to crystallize in a perovskite structure by formulating the Goldschmidt tolerance factor α [15]. This factor follows a proportionality relation between the ionic radii of the perovskite structure, given by:

$$\alpha = \frac{R_A + R_X}{\sqrt{2}(R_B + R_X)} \tag{2.1}$$

It measures how well the big cation A fits the BX_6 octahedra. For the ideal perovskite structure, this factor should be 1. However, in practice, most structures yield

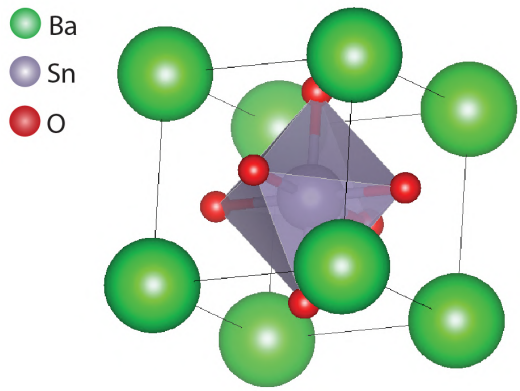

Figure 2.1: Crystal structure of $BaSnO_3$ within the primitive unit cell

a tolerance of 0.8 - 1.0. The Goldschmidt tolerance factor gives good agreement for oxide-perovskites, but it is not very accurate in predicting structures with more covalent bonds, such as halide-perovskites [16]. Therefore, various modified versions of this tolerance factor are adopted, taking into account the ionic radii and the oxidation state or the cation radii depending on the anion present in the composition; these curated tolerance factors have proven to yield more accurate predictions [17].

Perovskites can assume a variety of structures with diverse compositions due to the many plausible choices for the ions in the crystal. Perovskites can be classified into many categories depending on trends in these compositions. One such class of perovskites of particular interest are metal-inorganic perovskites. These compounds consist of A, typically a large alkali/alkaline earth metal cation (e.g., Cs^{+}, Ca^{+2}), B, a smaller transition metal ion or group - 13/14 cation (e.g., Pb^{+2}, Sn^{+2}) and X, an anion (e.g., Cl^{-}, Br^{-}, I^{-}, O^{-}). Depending on their anionic composition, these compounds can be further classified. Interesting subsets such as halide and oxide perovskites exhibit a deviation from the fundamental perovskite cubic structure due to octahedral distortions caused by the large A cation while maintaining the tolerance factor proportion. As a result, many of these materials adopt a pseudocubic structure at room temperature. Fig. (2.2) shows an orthorhombic $CsPbI_3$ structure (space group 62 *Pnma*). The structure is distorted to adopt an orthorhombic geometry with four formula units $Cs_4Pb_4I_{12}$ in the unit cell.

Metal oxide/halide perovskites have demonstrated remarkable potential in applications such as solar cells, memory devices, and superconductivity due to their attractive properties, including high light absorption, long carrier diffusion lengths, charge transport, and tunable bandgap [12]. These materials have record photovoltaic ef-

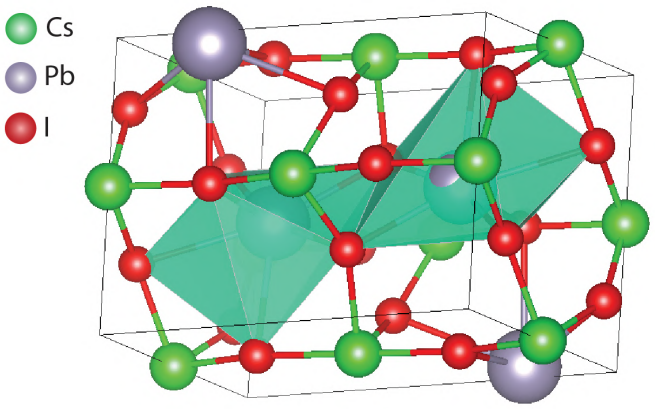

Figure 2.2: Crystal structure of γ - $CsPbI_3$, with 4 formula units inside the unit cell

ficiencies of more than 25%. Many metal inorganic perovskites are direct bandgap semiconductors, such as $LaInO_3$ and $CsPbI_3$. They can absorb visible and IR regimes of the electromagnetic spectra with very high optical absorption coefficients (order $10^4 - 10^5\,cm^{-1}$). This enables them to absorb light efficiently, even in thin-layer setups. These materials possess tunable band gaps, a crucial factor for applications.

In these systems, the valence-band maximum (VBM) is typically formed by the anti-bonding combination of metal s and anion p orbitals. In contrast, the conduction-band minimum (CBM) is controlled by the anti-bonding p orbitals of the metal and anion. Therefore, altering the energy of either the metal or the anionic orbitals can directly affect the material's band gap. Thus, the band gap can be curated by introducing dopants or substituting ions. For example, moving down a group (F, Cl, Br, I) increases the p orbital energy, raising the VBM and reducing the band gap energy. Similarly, substituting Pb with Sn raises the metal s orbital energy, reducing the band gap. The electronic positions of the B cation and the C anion significantly dictate the band structure and, therefore, the band gap of the materials. Additionally, structural differences in the larger cation A can alter the overlap between the metal s and anionic p orbitals, destabilising the VBM and leading to an adjusted band gap. These effects are essential to predict and validate the observed difference in band-gap for groups of materials with single ion variation like $CsPbI_3$ ($\approx$ 1.6 eV [18]) and $CsSnI_3$ ($\approx$ 1.4 eV [19])

Apart from their profound properties, these materials are also valuable because they can often be easily fabricated using solution-based processes such as spin-coating, inkjet printing, or slot-die coating [20]. However, most high-efficiency perovskites have only been fabricated on small-area modules ($< 1\ cm^2$), and these lab-scale deposition

processes are not yet ready for practical large-area devices (800 cm^2 – 14,000 cm^2). Large-area modules can be manufactured using blade coating, spray coating, and chemical vapour deposition techniques. These methods are still being developed to meet the demands of large-scale module production.

A major concern regarding perovskites is their chemical instability. Due to the ionic nature of the metal-anion bonds, many materials are prone to decompose when exposed to external conditions such as moisture, light, and air. Ongoing research involves compositional engineering to address this issue and improve their practical applications [21]. Another point of concern is the neurotoxicity of some of these materials. Lead-based perovskites have long been scrutinised for their potential to leak lead into the environment [22]. It is important to control the bioavailability of lead to prevent adverse effects of these perovskites. One straightforward solution is to replace Pb with elements like Sn, but it is crucial to maintain the balance as Pb-based perovskites are currently the most efficient variants. Li et al. [23] conducted a study comparing the bioavailability of SnI_2 and PbI_2. The study concluded that SnI_2 has a bioavailability ten times lower than PbI_2 due to the low water solubility of SnO, which is liberated upon the oxidation of PbI_2.

Modelling perovskites theoretically can be challenging due to their complex structures, high electron-phonon coupling, and rapid occurrence of phase transitions [24]. Perovskites often contain a large number of atoms in the unit cell and are frequently distorted (non-cubic), making them difficult and expensive to model using standard computational techniques. Additionally, many structures undergo phase transitions due to changes in temperature, pressure, or other stimuli. Therefore, a deeper understanding of the ground state system is necessary to optimise perovskite-based devices.

Table (2.1) provides a list of perovskite materials analysed in this project. We have focused on the polymorphs that are most stable at room temperature or have particular significance. Most of these systems follow the ideal cubic or distorted orthorhombic geometry.

System	**Geometry**	**Space group**
$BaSnO_3$	cubic	221-Pm3m
$LaInO_3$	orthorhombic	62-Pnma
γ - $CsPbI_3$	orthorhombic	62-Pnma
α - $CsPbI_3$	cubic	221-Pm3m
γ - $CsSnI_3$	orthorhombic	62-Pnma

Table 2.1: List of perovskites analysed

2.2 Wide-bandgap oxides

Wide band gap oxides are metal-oxide systems with a significant band gap (typically > 3 eV), imparting them the ability to withstand very high electric fields and transparency in the visible spectrum [25]. The large bandgap makes these materials inherently excellent insulators/semiconductors. Fig. (2.3) shows an example structure of a well studied wide bandgap oxide: β-Ga_2O_3. It is a monoclinic structure (space group C2/m) and is the most stable polymorph of Ga_2O_3 at room and high temperatures. The unit cell contains two formula units, each with two inequivalent Ga cations and three inequivalent O anions. One Ga ion occupies the tetrahedral site, and the other takes the octahedral site coordinated to four and six O ions, respectively. The inequivalence in the sites leads to strong anisotropy in the crystal, which is reflected in the effective mass results discussed later.

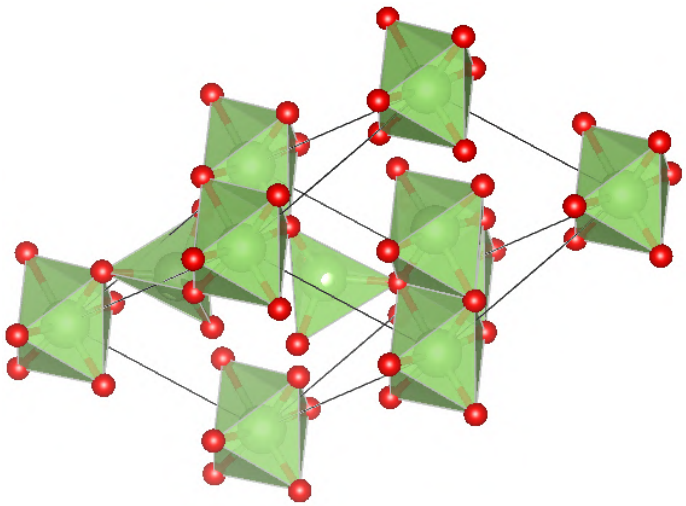

Figure 2.3: Monoclinic β-Ga_2O_3 crystal structure with two formula units

Ultrawide-bandgap (UWBG) materials are frequently optically transparent and possess good electrical conductivity, making them crucial for optoelectronic devices such as LCD and OLED displays, solar cells, and more. Although oxides are often recognised for their extensive electrical and thermal applications, they are also being investigated for their diverse range of adjustable properties [26]. These properties range from insulating to semiconducting and superconducting, as well as exhibiting piezo-/ferro- and antiferroelectric behaviour.

The unique electronic structure of these materials is crucial to their growing success. The conduction band (CB) of these materials consists of empty s-orbitals of post-

transition metals, while the valence band (VB) is occupied by oxygen $2p^6$ states. The optimal overlapping of the large (n > 4) s-orbitals results in high electron mobility and dopability, allowing for higher electron density [27]. The high dopability and electron mobility of these systems offer opportunities to explore defect-induced physics and make them a promising alternative to traditional Si-based semiconductors.

Table (2.2) provides a comprehensive list of the oxide systems analysed in this study, focusing on the most stable and significant polymorphs. For instance, Ga_2O_3 transitions between six polymorphs [28].

System	**Geometry**	**Space group**
β - Ga_2O_3	monoclinic	12-C2/m
α - Al_2O_3	trigonal	167-R/3c
ZrO_2	monoclinic	14-$P2_1/c$

Table 2.2: List of wide-bandgap oxides analysed

Chapter 3

Theoretical framework

DFT has been established as the most widely used *ab initio* technique for modelling and understanding the electronic structure of many-body systems and is considered a stalwart for such investigations.

Considering the many-body Hamiltonian:

$$H_{tot} = -\sum_{I} \frac{\hbar^2}{2M_I}\nabla^2_{\mathbf{R}_I} - \sum_{i} \frac{\hbar^2}{2m_e}\nabla^2_{\mathbf{r}_i} + \frac{1}{2}\sum_{I,J} \frac{Z_I Z_J e^2}{|\mathbf{R}_I - \mathbf{R}_J|} + \frac{1}{2}\sum_{i,j} \frac{e^2}{|\mathbf{r}_i - \mathbf{r}_j|} - \sum_{I,i} \frac{Z_I e^2}{|\mathbf{R}_I - \mathbf{r}_i|} \tag{3.1}$$

where: I, J are indices representing the nuclei and $\mathbf{R}_I$ and M_I corresponds to the position and mass of the nuclei, i, j represent the electrons and $\mathbf{r}_i$ and m_e corresponds to the position and mass of the electrons. Consequently, the first term gives the kinetic energy of the nuclei; the second gives the kinetic energy of the electrons; the third gives the potential energy of the Coulomb interaction between two nuclei; and the fourth term gives the electron-electron interaction potential. The last term gives the nucleus-electron interaction potential.

While in principle the solution of Eq. (3.1) would offer a comprehensive insight into the system, the inherent complexity of the problem renders its practical solution unfeasible, except for relatively simple systems. The Born-Oppenheimer(BO) approximation simplifies the problem by assuming the electrons to be moving in a static external potential $\mathrm{V_{ext}}(\mathbf{r})$ exerted by the nuclei; this assumption is based on the idea that since the nuclei are much heavier than the electrons, the movement of nuclei can be considered as negligible in comparison to the electrons [29].

Considering the BO approximation, the modern DF formalism (Kohn-Sham DFT) stems from the Hohenberg-Kohn theorems formulated in 1964, the first part of which states that all ground state properties for an electronic system in an external field

can be determined by knowing the electronic density distribution $\mathrm{n}(\mathbf{r})$ alone. The second part indicates the existence of a universal Functional $\mathrm{F}[\mathrm{n}(\mathbf{r})]$ of the electronic density, such that by variational principle, the global minimum of this functional $\mathrm{E}[\mathrm{n}(\mathbf{r})] = \int \mathrm{n}(\mathbf{r})\, \mathrm{V}_{\mathrm{ext}}\, \mathrm{d}\mathbf{r} + \mathrm{F}[\mathrm{n}(\mathbf{r})]$ gives the exact ground state energy E_0 and thereby the exact electronic density n_0 of the system [5].

Although the HK theorem indicates the existence of a density functional, this functional was still unknown. This problem was circumvented by Kohn and Sham in 1965. KS-DFT introduces an ansatz to mimic a complex many-body problem by an auxiliary system independent single-particle problem, assuming both systems have the same ground state density [30].

The Hamiltonian for this fictitious auxiliary system H_{KS} is given by:

$$\hat{H}_{KS} = -\frac{1}{2}\nabla^2 + V_{KS}(\mathbf{r}) \tag{3.2}$$

This system portrays a system of N independent electrons subjected to an effective potential V_{KS}; therefore, the ground state can be obtained by solving the one-electron Schrodinger equations N times:

$$\left(\frac{1}{2}\nabla^2 + V_{KS}(\mathbf{r})\right)\psi_i(r) = \epsilon_i\, \psi_i(r) \tag{3.3}$$

Consequently, the density of the system is given by:

$$n(\mathbf{r}) = \sum_{i=1}^{N} |\psi_i(\mathbf{r})|^2 \tag{3.4}$$

which obeys particle conservation by the condition:

$$\int n(\mathbf{r})\, d\mathbf{r} = N \tag{3.5}$$

With these conditions established, the universal functional can be written in the form:

$$\mathrm{F}[\mathrm{n}(\mathbf{r})] = \mathrm{T}_{\mathrm{S}}[\mathrm{n}(\mathbf{r})] + \mathrm{E}_{\mathrm{H}}[\mathrm{n}(\mathbf{r})] + \mathrm{E}_{\mathrm{XC}}[\mathrm{n}(\mathbf{r})] \tag{3.6}$$

where the non-interacting kinetic energy H_{S} is given by:

$$\mathrm{T}_{\mathrm{S}}[\mathrm{n}(\mathbf{r})] = \frac{1}{2}\sum_{i=1}^{N} \int \psi_i^*(r)\, \nabla^2 \psi_i(\mathbf{r})\, d\mathbf{r} \tag{3.7}$$

and the electrostatic Hartree energy $\mathrm{E_H}$ is given by:

$$\mathrm{E_H[n(\mathbf{r})]} = \frac{1}{2}\int\int \frac{n(\mathbf{r})n(\mathbf{r}')}{|\mathbf{r}-\mathbf{r}'|}\,d\mathbf{r}d\mathbf{r}' \tag{3.8}$$

and the exchange-correlation energy $\mathrm{E_{XC}}$ contains all the many-body corrections with respect to the independent particle approximation. To detail, it accounts for the correlation, the exchange and the difference between the independent and the many-body kinetic energy:

$$\mathrm{E_{XC}[n(\mathbf{r})]} = \mathrm{T[n(\mathbf{r})]} + \mathrm{T_S[n(\mathbf{r})]} + \mathrm{E_{int}[n(\mathbf{r})]} - \mathrm{E_H[n(\mathbf{r})]} \tag{3.9}$$

In principle, an exact $\mathrm{E_{XC}}$ term would give the exact ground state energy, but, in practice, this term has to be approximated by using exchange-correlation functionals, because the form of the correlation energy and the many-body kinetic energy is unknown. However, the exchange form is known.

Using the HK-II theorem, we can minimise the total energy functional $\mathrm{E[n(\mathbf{r})]} = \mathrm{F[n(\mathbf{r})]} + \int n(\mathbf{r})\,\mathrm{V_{ext}}(\mathbf{r})\,d\mathbf{r}$ to get the ground state energy of the original system:

$$\delta\left[\mathrm{F[n(\mathbf{r})]} + \int n(\mathbf{r})\,\mathrm{V_{ext}}(\mathbf{r})\,d\mathbf{r} - \mu\left[\int n(\mathbf{r})\,d\mathbf{r} - N\right]\right] = 0 \tag{3.10}$$

meanwhile, the KS potential can be computed with the knowledge of the exchange-correlation functional:

$$\begin{aligned}\mathrm{V_{KS}}(\mathbf{r}) &= \mathrm{V_{ext}}(\mathbf{r}) + \mathrm{V_H}(\mathbf{r}) + \mathrm{V_{XC}}(\mathbf{r}) \\ &= \mathrm{V_{ext}}(\mathbf{r}) + \frac{\delta \mathrm{E_H}[n(\mathbf{r})]}{\delta n(\mathbf{r})} + \frac{\delta \mathrm{E_{XC}}[n(\mathbf{r})]}{\delta n(\mathbf{r})} \\ &= \mathrm{V_{ext}}(\mathbf{r}) + \int \frac{n(\mathbf{r}')}{|\mathbf{r}-\mathbf{r}'|}\,d\mathbf{r}' + \frac{\delta \mathrm{E_{XC}}[n(\mathbf{r})]}{\delta n(\mathbf{r})}\end{aligned} \tag{3.11}$$

It is to be noted that $\mathrm{V_{KS}}(\mathbf{r})$ needs to be solved self-consistently as it $\mathrm{V_{KS}}(\mathbf{r})$ depends on the density through Eq. (3.11) and the density depends on $\mathrm{V_{KS}}(\mathbf{r})$ through Eq. (3.3-3.4). These equations together formulate the celebrated KS equations.

3.1 Basis functions: (L)APW+(lo)

Practically, while solving the KS equations (Eq. (3.3) numerically, a big task is modelling the wavefunction efficiently; therefore, the choice of basis functions (ψ_i) greatly affects the output of DFT calculations. Our ultimate goal is to solve it with a continuous and accurate wavefunction. For this purpose, we need a basis function that

expands such a wave function.

$$\left[-\frac{1}{2}\nabla^2 + \upsilon_{KS}(\mathbf{r})\right]\psi_{i\mathbf{k}}(\mathbf{r}) = \epsilon_{ik}\psi_{i\mathbf{k}}(\mathbf{r}) \tag{3.12}$$

Augmented Plane Waves (APW) based methods are considered the *gold standard* of DFT for investigating periodic systems because of their high accuracy [1]. The unit cell is sectioned in nuclei-centered muffin-tins (MT) and the interstitial (I) region. There are various techniques for introducing linearization in these functions, and we focus our attention on Linearized Augmented Place Waves (LAPW) + local orbital (lo) basis. To understand the significance of the (L)APW+lo basis set, we must first consolidate the utility of the APW basis, which implements a linear combination of atomic orbitals as the wave function.

$$\psi_{i\mathbf{k}}(\mathbf{r}) = \sum_{\mathbf{G}} C^{\mathbf{k}}_{i\mathbf{G}}\,\phi_{\mathbf{G}+\mathbf{k}}(\mathbf{r}) \tag{3.13}$$

where $\phi_{\mathbf{G}+\mathbf{k}}(\mathbf{r})$ are the APW, which are defined inside an effective atom (muffin tin) and in between the atoms (interstitial region) as:

$$\phi_{\mathbf{G}+\mathbf{k}}(\mathbf{r}) = \begin{cases} \sum_{lm} A^{\mathbf{G}+\mathbf{k}}_{lm\alpha}\, u_{l\alpha}(\mathbf{r}_\alpha)\, Y_{lm}(\hat{\mathbf{r}}_\alpha) & \text{for } \mathbf{r}_\alpha \leq R \\ \frac{1}{\sqrt{\Omega}}\, e^{i(\mathbf{G}+\mathbf{k})\,\mathbf{r}} & \text{for } \mathbf{r} \in I \end{cases} \tag{3.14}$$

This approach aptly describes the interstitial region between the atoms where the wave function is slow and smooth and the region within the muffin tin where it exhibits strong variations. Although the resultant basis set is small and enables inexpensive computation, the APW basis is inaccurate in practice. Moreover, the factors $A_{lm\alpha}$ are chosen such that the wavefunction is smooth at the muffin-tin and interstitial interface.

Using the definition (3.13), we can convert the differential KS equation (3.3) into an eigenproblem:

$$\sum_{\mathbf{G}'}(H^{\mathbf{k}}_{\mathbf{G}\mathbf{G}'} - \epsilon_{\mathbf{G}}\, S^{\mathbf{k}}_{\mathbf{G}\mathbf{G}'})\, C^{\mathbf{k}}_{\mathbf{G}'} = 0 \tag{3.15}$$

where the Hamiltonian is:

$$H^{k}_{\mathbf{G}\mathbf{G}} = \langle\phi_{\mathbf{G}+\mathbf{k}}| - \frac{1}{2}\nabla^2 + \upsilon_{KS}(\mathbf{r})\,|\phi_{\mathbf{G}+\mathbf{k}}\rangle \tag{3.16}$$

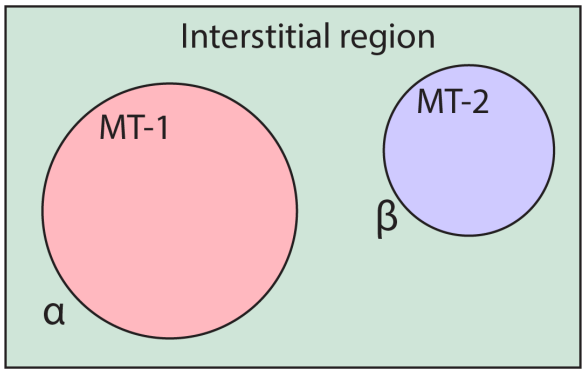

Figure 3.1: Muffin tin diagram for two species α and β

and the overlap matrix is given by:

$$S^{\mathbf{k}}_{\mathbf{GG}} = \langle \phi_{\mathbf{G+k}} | \phi_{\mathbf{G+k}} \rangle \tag{3.17}$$

and $C'^{k}_{\mathbf{G}}$ are the coefficients satisfied by Eq. (3.13). A plain look at this equation indicates the obvious problem: both the Hamiltonian and overlap matrices are energy dependent as per the definition of APW functions and are very non-trivial to solve. Hence, we notice that although APWs are a good approximation, the non-linearity of the energy parameter makes it a complex choice. To counter this problem, the energy dependence is linearized, which leads to the following radial function:

$$u_{l\alpha}(\mathbf{r}_\alpha; \epsilon) = u_{l\alpha}(\mathbf{r}_\alpha; \epsilon_{l\alpha}) + (\epsilon_{l\alpha} - \epsilon)\, \dot{u}_{l\alpha}(\mathbf{r}_\alpha; \epsilon_{l\alpha}) \tag{3.18}$$

Although the energy dependence still persists, this gives us the criteria that $u_{l\alpha}(\mathbf{r}_\alpha; \epsilon_{l\alpha})$ needs to be searched in $\dot{u}_{l\alpha}(\mathbf{r}_\alpha; \epsilon_{l\alpha})$. To implement this linearization technique, we introduce the LAPW basis. One particular representation of which within a particular muffin-tin α is:

$$\phi_{\mathbf{G+k}}(\mathbf{r}) = \sum_{lm} [A^{\mathbf{G+k}}_{lm\alpha}\, u_{l\alpha}(\mathbf{r}_\alpha; \epsilon_{l\alpha}) + B^{\mathbf{G+k}}_{lm\alpha}\, \dot{u}_{\mathbf{r}\alpha}(\mathbf{r}_\alpha; \epsilon_{l\alpha})]\, Y_{lm}(\hat{\mathbf{r}}_\alpha) \tag{3.19}$$

where the coefficients are computed by matching the planewaves at the muffin-tin boundary. Hence, this basis function is constrained to be smooth and continuous at the muffin tin boundary. These basis functions are very helpful, but they scale highly with decreasing the size of muffin-tin radii.

An alternative solution to the linearization problem is the local orbital basis. This can be defined as:

$$\phi_\mu = \begin{cases} \delta_{\alpha\alpha_\mu}\delta_{ll_\nu}\delta_{mm_\mu}\left[a_\mu u_{l\alpha}(r_\alpha;\epsilon_{l\alpha}) + b_\mu\, \dot{u}_{l\alpha}(r_\alpha;\epsilon_{l\alpha})\right] & r_\alpha \leq R \\ 0 & r \in I_\alpha \end{cases} \tag{3.20}$$

These functions are defined for a particular muffin tin and are zero everywhere else, and the coefficients follow the conditions: $\phi_\mu(r) = 0$ and $\int_\Omega |\phi_\mu|^2 dr = 1$. Since these functions strictly exist within a muffin-tin, they can be combined with APW basis functions to define a complete wavefunction in the form:

$$\psi_{i\mathbf{k}}(\mathbf{r}) = \sum_{\mathbf{G}} C^{\mathbf{k}}_{i\mathbf{G}}\phi_{\mathbf{G}+\mathbf{k}}(\mathbf{r}) + \sum_{\mu} C^{\mathbf{k}}_{i\mu}\phi_\mu(\mathbf{r}) \tag{3.21}$$

The wavefunction takes the following form within a particular MT:

$$\psi_{i\mathbf{k}}(\mathbf{r}) = \sum_{lm}\left[c^{i\mathbf{r}}_{lm}\, u_{l\alpha}(\mathbf{r}_\alpha;\epsilon_{l\alpha}) + d^{i\mathbf{k}}_{lm\alpha}\, \dot{u}_{l\alpha}(\mathbf{r}_\alpha;\epsilon_{l\alpha})\right] Y_{lm}(\hat{\mathbf{r}}_\alpha) \tag{3.22}$$

This definition greatly resembles the definition (3.19) for LAPW, and the coefficients must follow the same smoothness and continuity criteria as the LAPW but are more flexible as they combine different basis functions.

In principle, both LAPW and APW+lo are good basis functions, but the latter comes with a drawback: it uses an increased number of basis functions; therefore, they must be implemented carefully, bearing in mind the problem's computational complexity. Another advantage of using the latter is that they work well for describing semi-core states [31].

3.2 Exchange-Correlation Functionals

Returning to the energy expression in Eq. (3.6), the E_{xc} term encapsulates the exchange and correlation effects of the system. Exchange here implies the electron-electron exchange per the Pauli-exclusion principle, and the latter refers to the electron-electron repulsions beyond the Pauli-exclusion principle.

As aforementioned, since an exact solution of the E_{xc} is unknown, it must be approximated with an exchange-correlation (xc) functional of the electron density. There are several routes for approximating the energy term; therefore, functionals can be categorised based on their approximation method. There has been considerable research in the last 30 years concerning different facets of xc-functionals: (i) Developing more intricate and accurate functionals albeit at high computational consumption, (ii) Developing cheap, hence faster functionals, which led to the initial rise to popularity for

DFT. Perdew did an apt representation of these functionals by arranging them into a ladder of approximations, with each rung consisting of functionals following a similar approximation scheme [32].

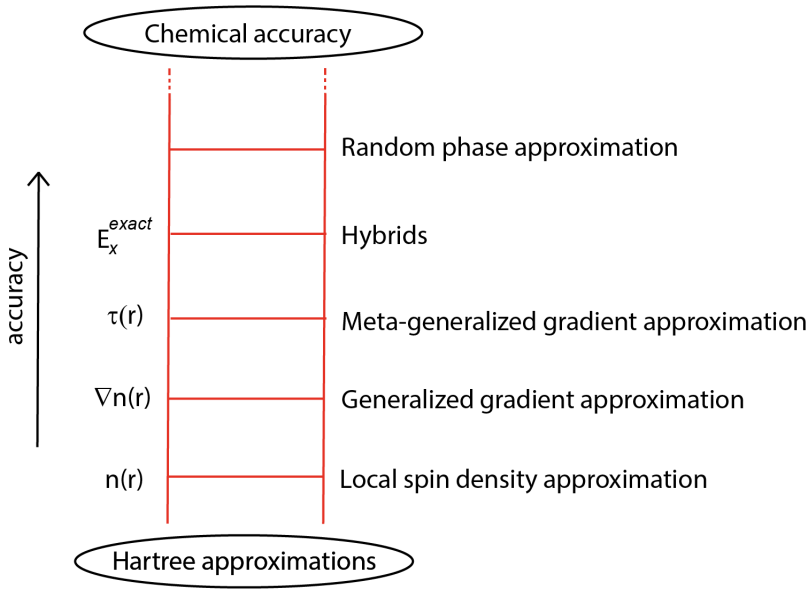

Figure 3.2: A 'Jacobs ladder' for categorising functionals according to their accuracy and complexity

As we move up the ladder, the functionals become more sophisticated and accurate but computationally expensive. Some 'rungs' of particular interest to us are:

- Local (spin) density approximation (LDA): This is the lowest rung of the ladder, and hence the cheapest type of xc-functional. The system is approximated by considering the xc-energy of an electron at point $\mathbf{r}$ to be the same as a homogeneous electron gas with the same electron density at point $\mathbf{r}$ and hence, it exclusively depends on n($\mathbf{r}$) [33] as:

$$E_{xc}^{\mathrm{LDA}}[n(\mathbf{r})] = \int dr\ n(\mathbf{r})\, \epsilon_{xc}^{\mathrm{unif}}(n(\mathbf{r})) \tag{3.23}$$

  An obvious advantage of the LDA is its simplicity, ignoring the correction to the xc-energy stemming from the inhomogeneities of the electron density. Still, it is very successful and even produces good results in systems where the electron density has high variation. However, bad approximation of the ground state and binding energies makes large errors in predicting the energy gaps of many materials. It is hence viewed as a cheap and convenient xc-functional.

- Generalised gradient approximation (GGA): These approximations compensate for the missing correction terms of LDA by incorporating an extra layer of information in the form of the gradient and higher spatial derivatives of the electron density [34].

$$E_{xc}^{\mathrm{GGA}}[n\mathbf{r}] = \int d\mathbf{r}\; n(\mathbf{r})\, \epsilon_{xc}^{\mathrm{GGA}}(n(\mathbf{r}), \nabla n(\mathbf{r})) \tag{3.24}$$

  This new layer of information gives better results than the LDA generally, only overestimating results for ionic crystals where the LDA gives a better fit for the lattice constants. However, both of these functionals are constrained to systems with low localised charges and correlation, and hence, beyond LDA and GGA approximations are sought.

- Hybrid density functionals: These functionals combine exact exchange from Hartree-Fock (HF) theory with GGA functionals to carefully combine local and non-local effects in the approximation [35]. HF theory fails to represent the correlation amongst the electrons, thereby failing significantly for computing properties where this overestimation of ionic character yields bad results, e.g., the bandgap of semiconductors. Similarly, as aforementioned, LDA and GGA functionals also fail to estimate such quantities, especially the error in determining semiconductor band gaps. GGA and HF methods were observed to give errors of opposite signs concerning experimental data. Therefore, it was only a pragmatic thought to balance these errors by combining results from both theories.

$$E_{xc}^{\mathrm{hybrid}} = E_{xc}^{\mathrm{GGA}} + \alpha(E_{x}^{\mathrm{exact}} - E_{x}^{\mathrm{GGA}}) \tag{3.25}$$

  where α is the exact exchange mixing ratio, it is a non-empirical parameter, the value of which is altered to obtain a balance between optimal results and computational resources [36]. PBE0 and HSE06 are two of the most popular hybrid XC-functionals.

  The PBE0 XC-functional combines the GGA-PBE exchange energy with the HF exchange. The standard mixing parameter is generally considered to be 0.25 [37]. HSE (Heyd-Scuseria-Ernzerhof) is another hybrid functional similar to PBE0, but it incorporates the correction in exact exchange by breaking it into a short-range part (PBE-like) and a long-range part (exact HF-like); both these parts are weighed in by an extra parameter ω [38]. The values of these parameters can be altered based on non-empirical requirements; however, the standard chosen for HSE06 is $\alpha = 0.25$ and $\omega = 0.11$.

Chapter 4

Methodology

4.1 Computational Framework

To compute highly precise ground-state DFT calculations, choosing an appropriate DFT implementation is necessary. There are codes available based on methods such as pseudopotentials and projector-augmented waves [39, 40]. However, it has been established that full-potential all-electron codes are generally more accurate. As seen in section (3.1), the choice of basis function directly impacts the modelling of the wavefunction and, therefore, the solution of the KS Hamiltonian. We also saw the utility of using the Linearized augmented planewave and local orbital method in the DF formalism [41, 42]. It has been documented that the LAPW+lo method is often trusted blindly for validating pseudopotential-based implementations [43].

Figure 4.1: **exciting** used for DFT calculations and NOMAD used for uploading calculations [1, 2].

In this context, we used **exciting** for our calculations. **exciting** is a full potential all-electron code based on plane-wave augmentation implementing different flavours of the Linearized augmented plane waves + local orbitals (LAPW+lo) method [1]. A big advantage of all-electron codes is their ability to treat all sets of electrons equally

without freezing core electronic states like pseudopotentials. This allows for separate basis functions for core and valence electrons, making it efficient to model high-energy states. The code uses augmented plane waves for the muffin tin and interstitial regions with linearised energies. It can implement auxiliary local orbitals for particular muffin tins, combining the best of both worlds. It has been documented that **exciting** can reach a precision as high as 1 microHa/atom, making it an excellent choice for our purpose [43].

We use NOMAD to document and publish our results (Fig. (4.1)). NOMAD is an online repository of electronic structure calculations for managing FAIR (i.e., Findable, Accessible, Interoperable, and Reuseable) data. It supports several codes, including **exciting**, allowing to automatically parse and process the data and the results [2].

4.2 Workflow

Planning a straightforward and linear workflow is essential for this project, as it requires iterative computations over our chosen system and XC-functional pool. Fig. (4.2) presents a schematic of our workflow, which is discussed in detail in the following subsections.

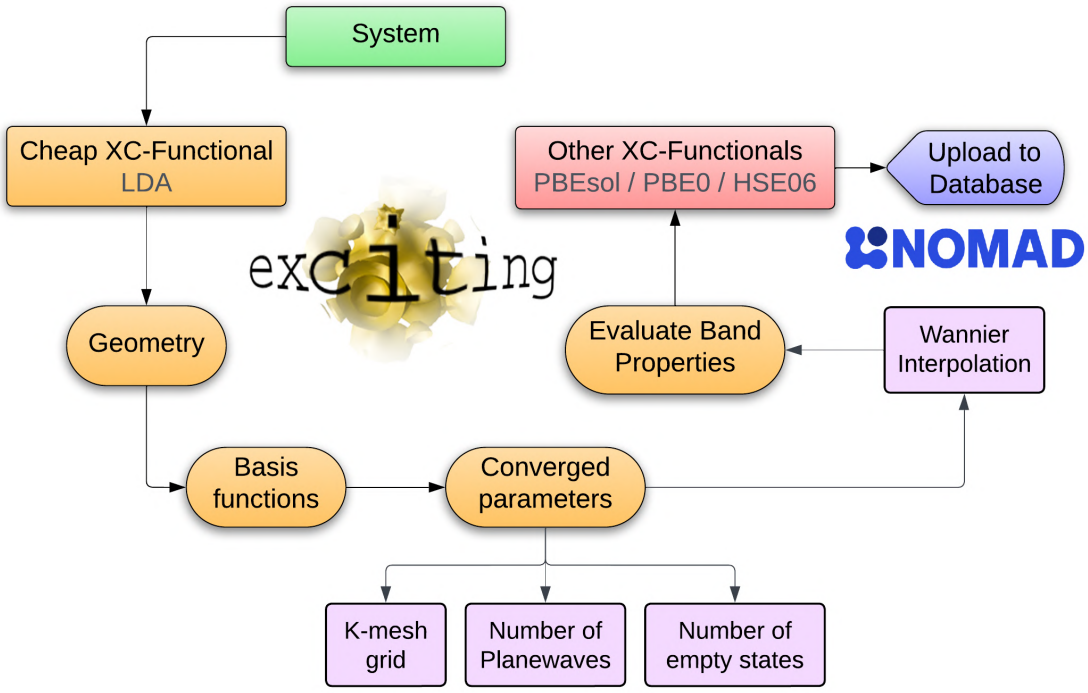

Figure 4.2: An exhaustive workflow showcasing all steps involved in our computations and analysis

4.2.1 Fixing the structure

We start by selecting a structure from the system pool and run our protocol. Choosing a well-represented geometry is very important. We usually start with experimental data or PBE-optimised geometry. GGA-PBE XC-functional is known to generate good lattice parameters without being too expensive. The geometry is defined in **exciting** by specifying the unit cell basis vectors and atomic coordinates. Consider the example of α - $CsPbI_3$, which is a cubic system, hence the lattice parameters: a = b = c and $\alpha = \beta = \gamma = 90°$, giving the basis vectors 100, 010 and 001. The Cs atom occupies the body-centred position ($\frac{1}{2}$,$\frac{1}{2}$,$\frac{1}{2}$); Pb at the corner: (0,0,0) and 3 oxygen atoms at the edge centres: ($\frac{1}{2}$,0,0) (0,$\frac{1}{2}$,0) (0,0,$\frac{1}{2}$).

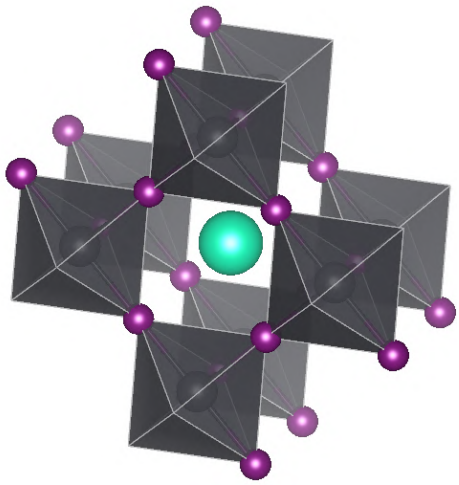

Figure 4.3: Crystal structure of α - $CsPbI_3$

4.2.2 Constructing a good basis set

This step is crucial for ensuring the numerical precision of our calculations. The recipe for modifying our basis is based on a former study by Gulans et al. [43] which aimed to achieve microhartree precision for atoms, molecules, and periodic systems. It has been illustrated that using auxiliary local orbitals in the basis set for increasing values of angular momenta results in exact total energies. As local orbitals are useful for modelling unoccupied states, we classify additional electrons to be treated as semi-core and valence.

Another critical factor is the choice of appropriate linearisation energies in Eq. (3.18) so that the self-consistent cycle converges to accurate values. This can be done using Wigner - Seitz rules but must be carefully curated for each local orbital, as an

inappropriate value can cause the self-consistent cycle to diverge.

Therefore, we can summarise our fundamental recipe by the following steps:

- Increasing the number of semi-core and valence states
- Treating these states with additional local orbitals, up to higher l-channels
- Choosing well-approximated trial energies

The code snippet below demonstrates the example of the Barium element in the case of $BaSnO_3$. First, we select the core states, which are typically limited to the 4p orbitals. However, we expand the number of semi-core and valence states by including the 4s and 4p electrons as non-core. This is necessary to incorporate the local orbitals and outer valence electrons for these electrons.

```
<atomicState n="1" l="0" kappa="1" occ="2.00000" core="true"/>
<atomicState n="2" l="0" kappa="1" occ="2.00000" core="true"/>
<atomicState n="2" l="1" kappa="1" occ="2.00000" core="true"/>
<atomicState n="2" l="1" kappa="2" occ="4.00000" core="true"/>
<atomicState n="3" l="0" kappa="1" occ="2.00000" core="true"/>
<atomicState n="3" l="1" kappa="1" occ="2.00000" core="true"/>
<atomicState n="3" l="1" kappa="2" occ="4.00000" core="true"/>
<atomicState n="3" l="2" kappa="2" occ="4.00000" core="true"/>
<atomicState n="3" l="2" kappa="3" occ="6.00000" core="true"/>
<atomicState n="4" l="0" kappa="1" occ="2.00000" core="false"/>
<atomicState n="4" l="1" kappa="1" occ="2.00000" core="false"/>
<atomicState n="4" l="1" kappa="2" occ="4.00000" core="false"/>
<atomicState n="4" l="2" kappa="2" occ="4.00000" core="false"/>
<atomicState n="4" l="2" kappa="3" occ="6.00000" core="false"/>
<atomicState n="5" l="0" kappa="1" occ="2.00000" core="false"/>
<atomicState n="5" l="1" kappa="1" occ="2.00000" core="false"/>
<atomicState n="5" l="1" kappa="2" occ="4.00000" core="false"/>
<atomicState n="6" l="0" kappa="1" occ="2.00000" core="false"/>
```

Now, we define the basis functions for the element. A default LAPW basis is defined for all the core states. Then, we define a set of local orbitals for the s-orbitals (l=0), the trial energy for which is determined using the Wigner-Seitz rules. In this set, the first two local orbitals correspond to the 5s orbitals, and the value of the matching orders corresponds to the order of the derivatives according to the Eq. (3.18). In this case, the 5s and 6s orbitals are very similar and may overlap in the calculation, so we have not modelled the 6s states. The following function corresponds to a combination of the 5s and 4s orbitals. The following two local orbitals correspond to 4s orbitals, characterised by the deep trial energies used.

```
<default type="lapw" trialEnergy="0.1500" searchE="false"/>

<custom l="0" type="lapw" trialEnergy="-0.388" searchE="false"/>
<lo l="0">
  <wf matchingOrder="0" trialEnergy="-0.388" searchE="false"/>
  <wf matchingOrder="1" trialEnergy="-0.388" searchE="false"/>
</lo>
<lo l="0">
  <wf matchingOrder="1" trialEnergy="-0.388" searchE="false"/>
  <wf matchingOrder="2" trialEnergy="-0.388" searchE="false"/>
</lo>
<lo l="0">
  <wf matchingOrder="0" trialEnergy="-0.388" searchE="false"/>
  <wf matchingOrder="0" trialEnergy="-8.308" searchE="false"/>
</lo>
<lo l="0">
  <wf matchingOrder="0" trialEnergy="-8.308" searchE="false"/>
  <wf matchingOrder="1" trialEnergy="-8.308" searchE="false"/>
</lo>
<lo l="0">
  <wf matchingOrder="0" trialEnergy="-8.308" searchE="false"/>
  <wf matchingOrder="2" trialEnergy="-8.308" searchE="false"/>
</lo>
```

A similar set of local orbitals is implemented for the cases of l=1 and l=2. Since we aim to add local orbitals for higher l-channels, we also add functions for the unoccupied f-subshell. Below are the local orbitals with trial energies corresponding to the 4f orbitals.

```
<custom l="3" type="lapw" trialEnergy="0.784" searchE="false"/>
<lo l="3">
  <wf matchingOrder="0" trialEnergy="0.784" searchE="false"/>
  <wf matchingOrder="1" trialEnergy="0.784" searchE="false"/>
</lo>
<lo l="3">
  <wf matchingOrder="0" trialEnergy="0.784" searchE="false"/>
  <wf matchingOrder="2" trialEnergy="0.784" searchE="false"/>
</lo>
```

4.2.3 Convergence checks on parameters

A DFT calculation is influenced by several input parameters, such as the Brillouin zone sampling and the planewave cutoff. To obtain satisfactory results, it is necessary to perform tests to obtain a set of converged parameters. Our protocol involves running iterative calculations on one variable parameter at a time while keeping the other parameters fixed. We measure a particular observable for these iterations and analyze the results. We plot the error in the observable against the variable parameter to check the trend. The error is minimised against a specific threshold. When the threshold is met, the corresponding value qualifies as a converged value. It is important to check certain crucial parameters, such as:

- `ngridk`: Calculating many system properties requires directly solving integrals over the Brillouin zone, which can be cumbersome. Therefore, these integrals are approximated by sampling points on a grid in the reciprocal space, and this parameter defines the dimensions for k-space sampling. The more refined the k-grid vectors are, the better the calculation and the computational complexity scales linearly with this parameter. Fig. (4.4) shows an example of $\beta - Ga_2O_3$ with a cubic mesh ranging from (2, 2, 2) to (9, 9, 9); the error in total energy is plotted against the parameter value with energy corresponding to (10, 10, 10) taken as the reference. In this case, the convergence criteria are set to 10^{-4} Ha, making `ngridk` = (6, 6, 6) a good choice.

- `rgkmax`: concerning section (3.1), the eigenvalue KS Eq. (3.3) is made finite dimensional by keeping an upper bound cut-off on the $|G + k|$ vector: $|G + k| \leq G_{max}$ and this upper bound G_{max} is defined as the plane-wave cutoff. However, this is not a good measure of the basis set cutoff as it does not take into account the size of the muffin tin. Therefore, `rgkmax` is defined as the effective planewave cutoff `rgkmax` $= R_{MT}G_{max}$. The computation time for this parameter scales to the power of 9, which is very significant, so it is important to maintain a good balance between precision and resources. We follow a similar convergence check for this parameter as for `ngridk`.

- `nempty`: The parameter `nempty` determines the number of empty states and becomes a critical parameter in hybrid functional calculations due to the cumbersome computation of the non-local external potential V_{xnl}. The `nempty` is upper bounded by the Hamiltonian size, which depends on the number of plane wave functions and hence on the cutoff parameter: `rgkmax`. Therefore, converging `rgkmax` is important before converging `nempty`.

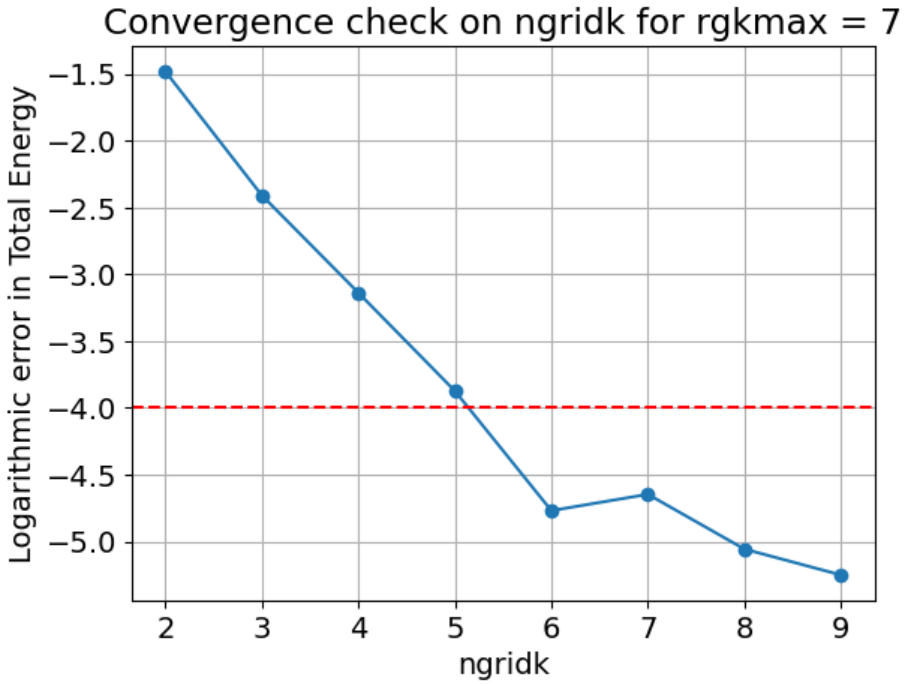

Figure 4.4: Plot showing convergence over `ngridk` parameter for `rgkmax`=7. The error in total energy is plotted on a log scale to check against the threshold of 10^{-4} Ha

4.2.4 Evaluating the electronic structure

A well-converged set of parameters equips us with all the necessary tools to perform preliminary calculations. We use an inexpensive LDA functional to generate the electronic band structure. We use the standard path to traverse k-points to compute the band structure [44]. Using β-Ga_2O_3 as an example, we consider the following bandpath to obtain the preliminary electronic structure. We then analyse the band structure to produce maximally localised Wannier functions by forming groups of isolated and entangled bands. Wannier functions provide an alternative approach to the usual Brillouin zone sampling and become very important for cases of hybrid functionals. With the maximally localised Wannier functions obtained, we now interpolate the wavefunction onto a much finer reciprocal space. This is an important step because some of these calculations are very expensive, and it is necessary to interpolate a sparse k-mesh to get precise band properties. We compute the wannier-interpolated band structure to analyse whether it overlaps with the ground state standard LDA band structure. Fig. (4.5) shows the change in band structure for the case of β-Ga_2O_3 using the LDA XC functional. It can be seen that the band is slightly smoother and overlaps closely with the regular band structure.

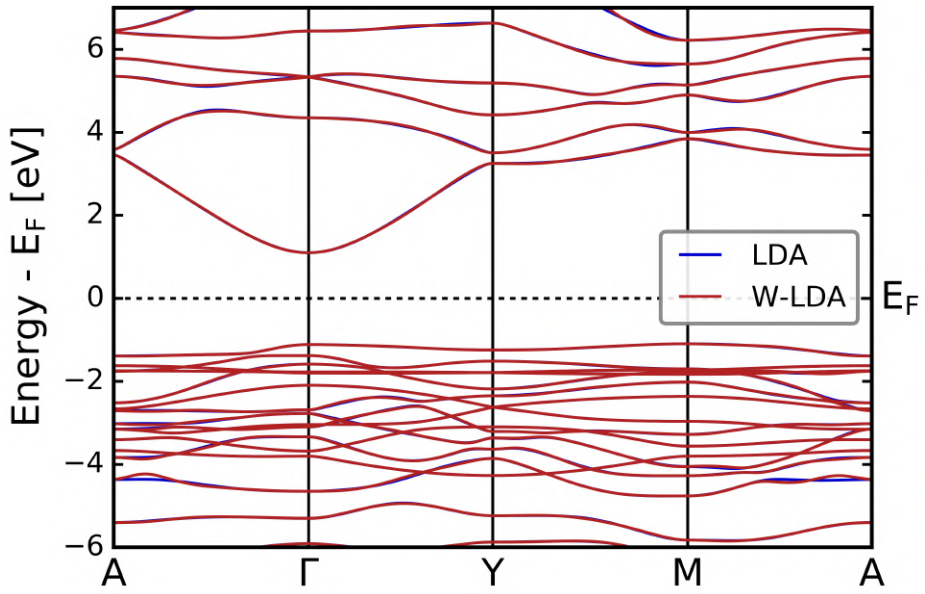

Figure 4.5: LDA bandstructure and Wannier interpolated LDA bandstructure plotted on top of each other

4.2.5 Documentation

After successfully interpolating the k-mesh, we can calculate other band properties. We calculate the electronic density of states and bandgap separately, and analyse the effective mass tensor by computing wannier functions at the band extremes. This completes the computation cycle for one system and an XC-functional combination. We repeat these steps for the other XC-functionals: PBEsol, PBE0 and HSE06.

After completing the aforementioned steps, we upload our calculations to NOMAD as a dataset, and the cycle re-iterates for the rest of the materials.

4.3 Other computational details

Efficient parallelisation of code and good computational resources are necessary for dealing with calculations involving detailed basis functions and parameters. **`exciting`** uses MPI and OpenMP parallelisation models, which must be carefully utilised to compute over shared and distributed memory efficiently. We use our computer cluster network for the calculations as well as external HPC facilities. We gratefully acknowledge the computing time made available on the high-performance computer "Lise" at the NHR Center NHR@ZIB (www.nhr-verein.de/unsere-partner). To effectively distribute the load between nodes, it is important to ensure that MPI and OpenMP ranks divide the total number of points in the reciprocal space. Addition-

ally, it is essential to ensure that the OpenMP ranks are coherent with the CPU architecture, i.e. they divide the number of cores in the CPU.

For example, in the case of γ - $CsPbI_3$, the (6x6x6) k-space is reduced to 20 points due to the system's symmetry. Therefore, we typically choose the following configuration to run the computation on a 36-core CPU: OpenMP threads = 9, MPI processes = 8, number of nodes = 2. This is a fair configuration as the Number of OpenMP times the number of MPI processes of a single node = the number of CPU cores available. Moreover, the OpenMP threads almost completely divide the number of points in the reduced reciprocal space. This example shows a basic scheme for effective calculation; however, in practice, a lot of other factors determine the distribution, such as the XC-functional used; for instance, hybrid functionals require computation of the non-local external potential V_{xnl} which depends on the full reciprocal space. Therefore, it is essential to perform scaling tests with small calculations and inexpensive parameters before committing to high resource usage.

Chapter 5

Results

This chapter presents the results of our computations for each material individually. As mentioned, we have computed the electronic band structure and density of states, the effective mass tensor and the electronic bandgap. With regards to the functionals used, we have performed LDA (LDA-PW [45]) and GGA (PBEsol [46]) calculations for all materials in our system pool and have performed the more expensive Hybrid calculations (PBE0 [47] and HSE06 [38]) for the case of $BaSnO_3$. We first present the results for $BaSnO_3$, followed by a side-by-side comparison of LDA and PBEsol calculations for all the other materials.

For plotting the electronic bandstructure, we have chosen the standard band paths as per this study highlighting tools for high-throughput electronic bandstructure calculations [48].

The bandgap is truncated to three decimal places to better model the minor difference between some calculations. The effective masses are represented in the tensorial form for both the VBM and CBM. These masses are calculated at the band extremes for both cases. In the case of degenerate bands we have compared one fixed tensor for every functional. Moreover, the values for each component have been truncated to two decimal places for better analysis by only comparing significant values.

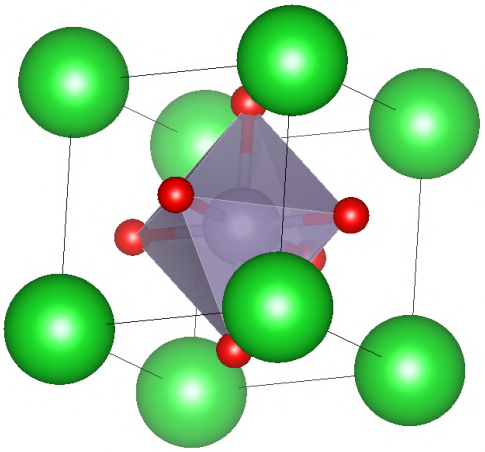

$BaSnO_3$

LDA $\rightarrow$ 0.821 eV	PBEsol $\rightarrow$ 0.902 eV
PBE0 $\rightarrow$ 3.420 eV	HSE06 $\rightarrow$ 2.693 eV

$$m^*_{\text{VBM}} : \text{LDA} \rightarrow \begin{bmatrix} -0.65 & 0 & 0.03 \\ 0 & -0.65 & -0.2 \\ 0.03 & -0.20 & -16.57 \end{bmatrix} \quad \text{PBEsol} \rightarrow \begin{bmatrix} -0.65 & 0 & -0.26 \\ 0 & -0.65 & -0.16 \\ -0.26 & -0.16 & -14.72 \end{bmatrix}$$

$$m^*_{\text{CBM}} : \text{LDA} \rightarrow \begin{bmatrix} 0.18 & 0 & 0 \\ 0 & 0.18 & 0 \\ 0 & 0 & 0.18 \end{bmatrix} \quad \text{PBEsol} \rightarrow \begin{bmatrix} 0.18 & 0 & 0 \\ 0 & 0.18 & 0 \\ 0 & 0 & 0.18 \end{bmatrix}$$

$$m^*_{\text{VBM}} : \text{PBE0} \rightarrow \begin{bmatrix} -0.74 & 0.02 & -0.88 \\ 0.02 & -0.67 & 0.21 \\ -0.88 & 0.21 & -12.07 \end{bmatrix} \quad \text{HSE06} \rightarrow \begin{bmatrix} -0.67 & 0.01 & -0.15 \\ 0.01 & -0.72 & 0.79 \\ -0.15 & 0.79 & -14.13 \end{bmatrix}$$

$$m^*_{\text{CBM}} : \text{PBE0} \rightarrow \begin{bmatrix} 0.21 & 0 & 0 \\ 0 & 0.21 & 0 \\ 0 & 0 & 0.21 \end{bmatrix} \quad \text{HSE06} \rightarrow \begin{bmatrix} 0.21 & 0 & 0 \\ 0 & 0.21 & 0 \\ 0 & 0 & 0.21 \end{bmatrix}$$

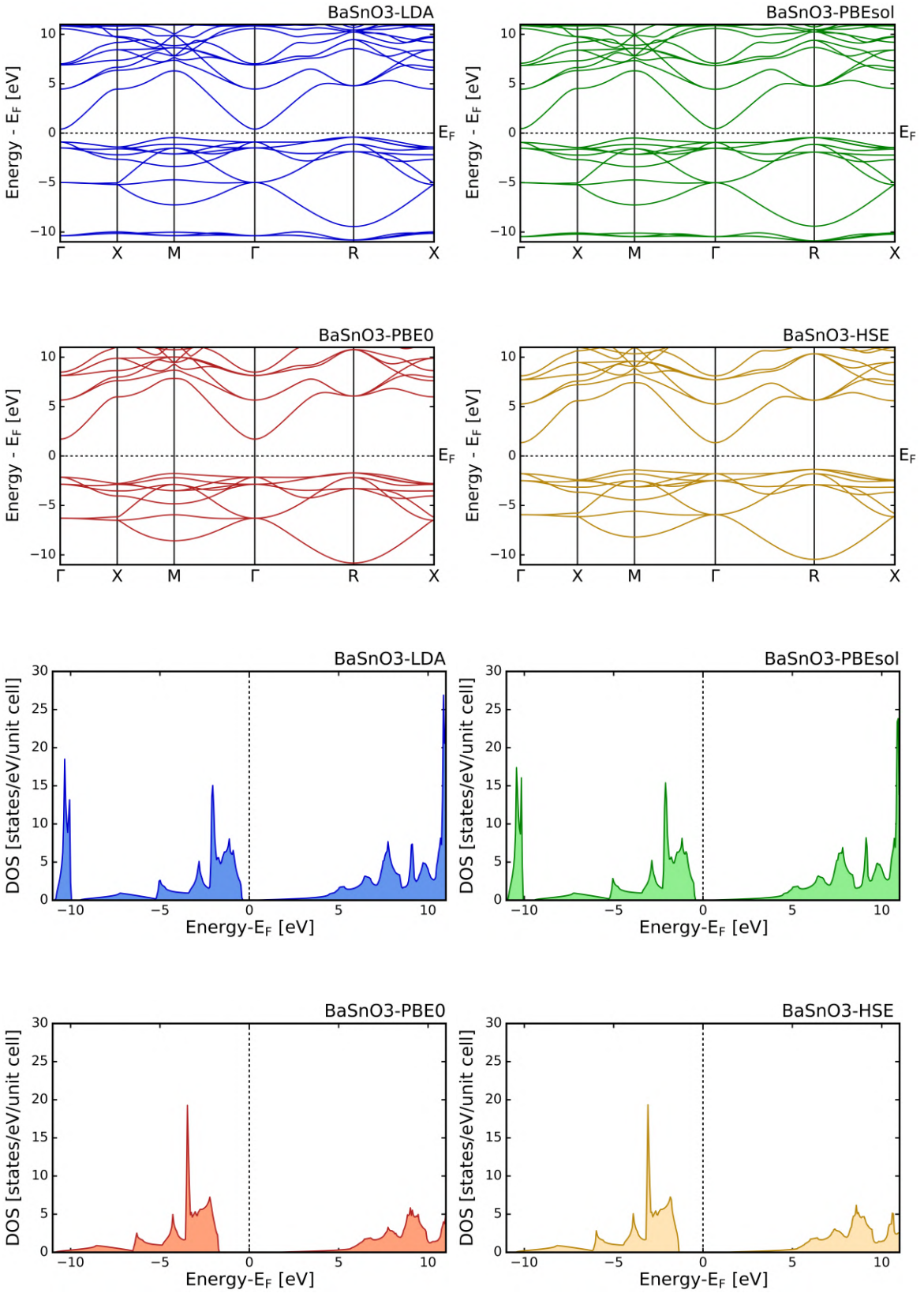
BaSnO3-LDA
BaSnO3-PBEsol
BaSnO3-PBE0
BaSnO3-HSE
Energy - E_F [eV]
E_F
Γ X M Γ R X
DOS [states/eV/unit cell]
Energy-E_F [eV]

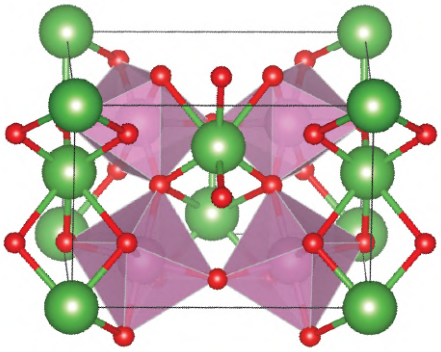

$LaInO_3$

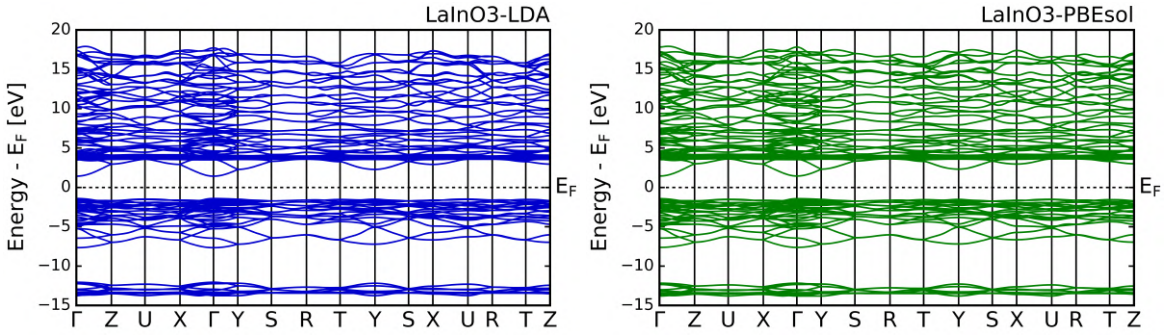

Bandgap: LDA $\rightarrow$ 2.831 eV | PBEsol $\rightarrow$ 2.870 eV

$$m^*_{\mathrm{VBM}} : \mathrm{LDA} \rightarrow \begin{bmatrix} -0.60 & 0 & 0 \\ 0 & -3.84 & 0 \\ 0 & 0 & -1.23 \end{bmatrix} \quad \mathrm{PBEsol} \rightarrow \begin{bmatrix} -0.56 & -0.17 & -0.02 \\ -0.17 & -3.87 & 0.01 \\ -0.02 & 0.01 & -1.22 \end{bmatrix}$$

$$m^*_{\mathrm{CBM}} : \mathrm{LDA} \rightarrow \begin{bmatrix} 0.41 & 0 & 0 \\ 0 & 0.51 & 0 \\ 0 & 0 & 0.53 \end{bmatrix} \quad \mathrm{PBEsol} \rightarrow \begin{bmatrix} 0.40 & 0 & 0 \\ 0 & 0.50 & 0 \\ 0 & 0 & 0.52 \end{bmatrix}$$

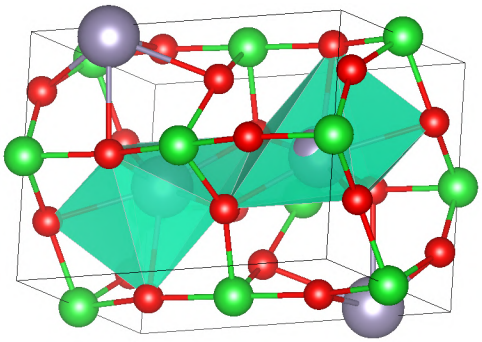

γ – $CsPbI_3$

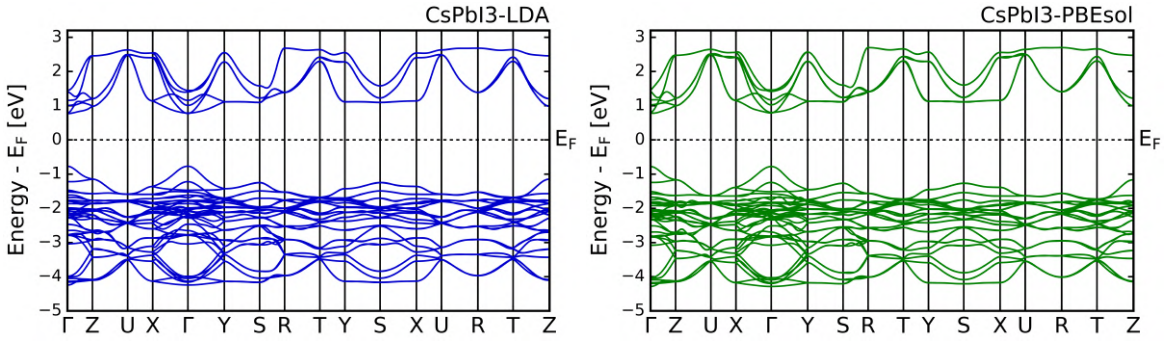

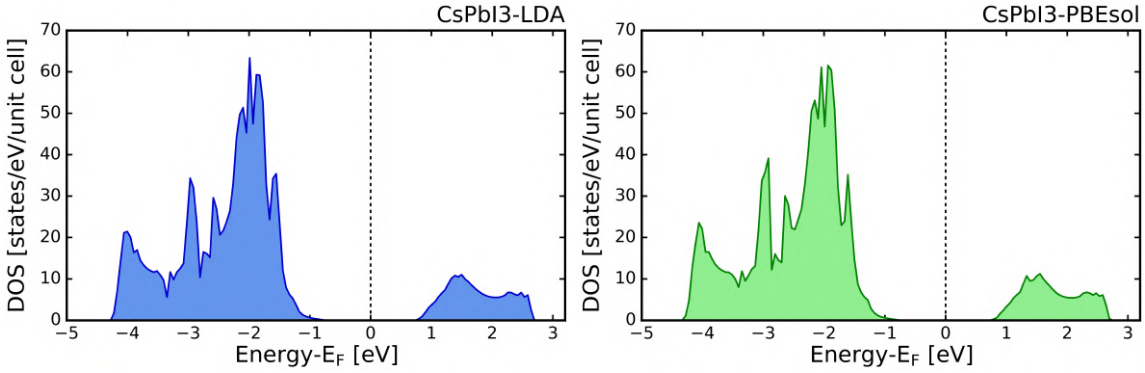

Bandgap: LDA → 1.540 eV | PBEsol → 1.555 eV

$$m^*_{\mathrm{VBM}} : \mathrm{LDA} \rightarrow \begin{bmatrix} -0.26 & 0 & 0 \\ 0 & -0.22 & 0 \\ 0 & 0 & -0.20 \end{bmatrix} \quad \mathrm{PBEsol} \rightarrow \begin{bmatrix} -0.26 & 0 & 0 \\ 0 & -0.22 & 0 \\ 0 & 0 & -0.20 \end{bmatrix}$$

$$m^*_{\mathrm{CBM}} : \mathrm{LDA} \rightarrow \begin{bmatrix} 0.16 & 0.01 & 0.01 \\ 0.01 & 0.15 & 0.02 \\ 0.01 & 0.02 & 0.43 \end{bmatrix} \quad \mathrm{PBEsol} \rightarrow \begin{bmatrix} 0.23 & 0.02 & -0.08 \\ 0.02 & 0.17 & -0.02 \\ -0.08 & -0.02 & 0.31 \end{bmatrix}$$

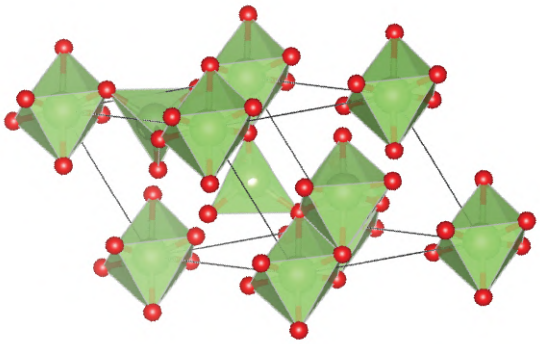

β - Ga_2O_3

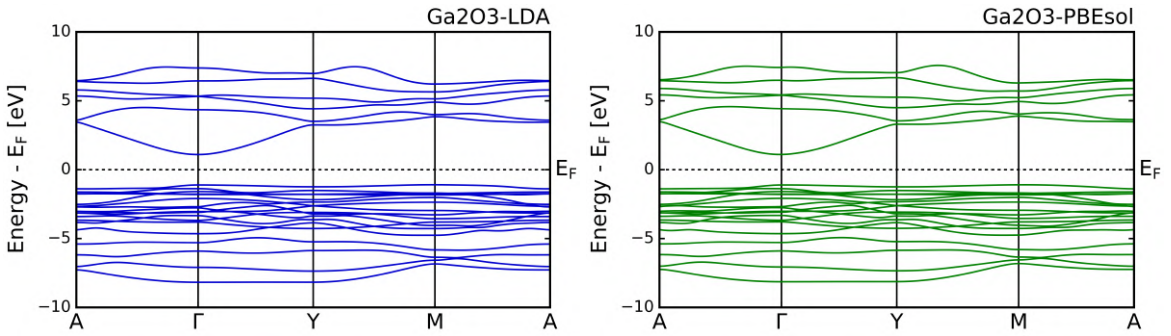

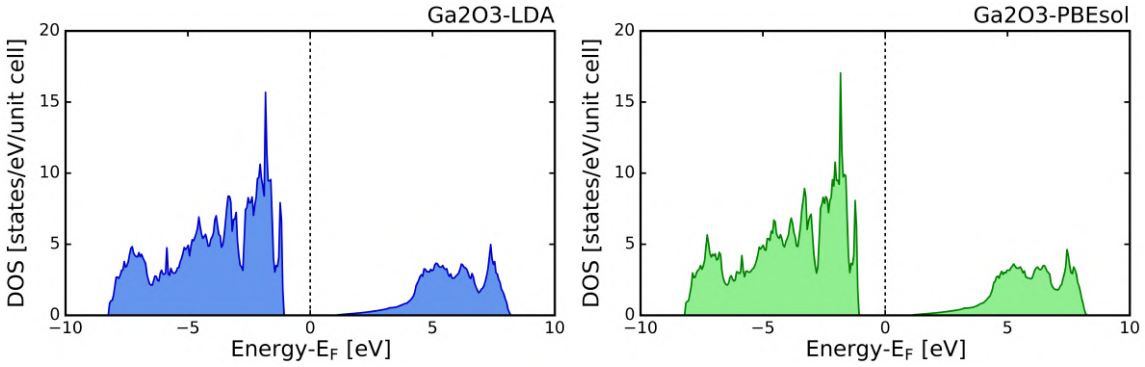

Bandgap: LDA $\rightarrow$ 2.177 eV | PBEsol $\rightarrow$ 2.183 eV

$$m^*_{\mathrm{VBM}} : \mathrm{LDA} \rightarrow \begin{bmatrix} -3.24 & -0.17 & -0.51 \\ -0.17 & -2.71 & -0.02 \\ -0.51 & -0.02 & -3.45 \end{bmatrix} \quad \mathrm{PBEsol} \rightarrow \begin{bmatrix} -3.21 & -0.09 & 0.48 \\ -0.09 & -2.70 & 0.20 \\ 0.48 & 0.20 & -3.79 \end{bmatrix}$$

$$m^*_{\mathrm{CBM}} : \mathrm{LDA} \rightarrow \begin{bmatrix} 0.31 & 0.02 & 0 \\ 0.02 & 0.25 & 0.05 \\ 0 & 0.05 & 0.24 \end{bmatrix} \quad \mathrm{PBEsol} \rightarrow \begin{bmatrix} 0.30 & 0 & -0.01 \\ 0 & 0.23 & 0 \\ -0.01 & 0 & 0.22 \end{bmatrix}$$

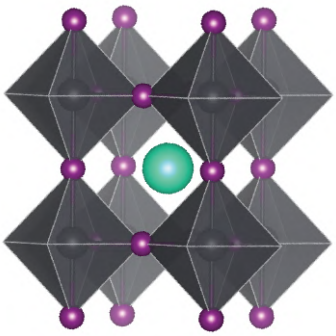

α – $CsPbI_3$

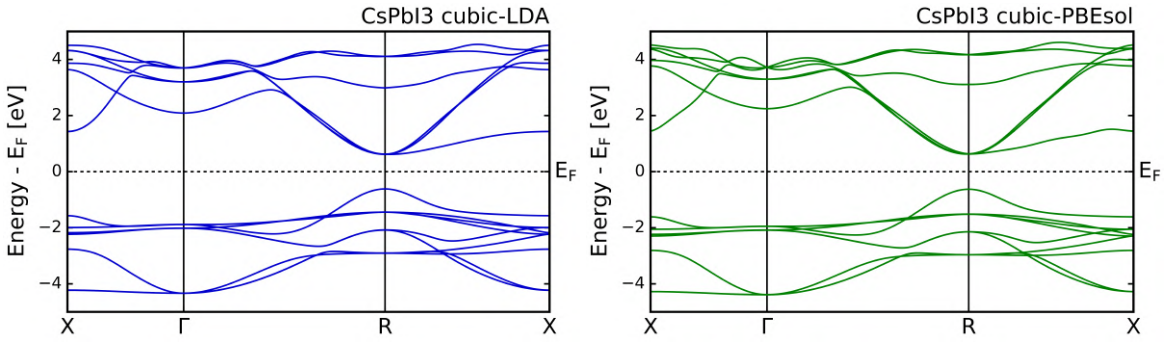

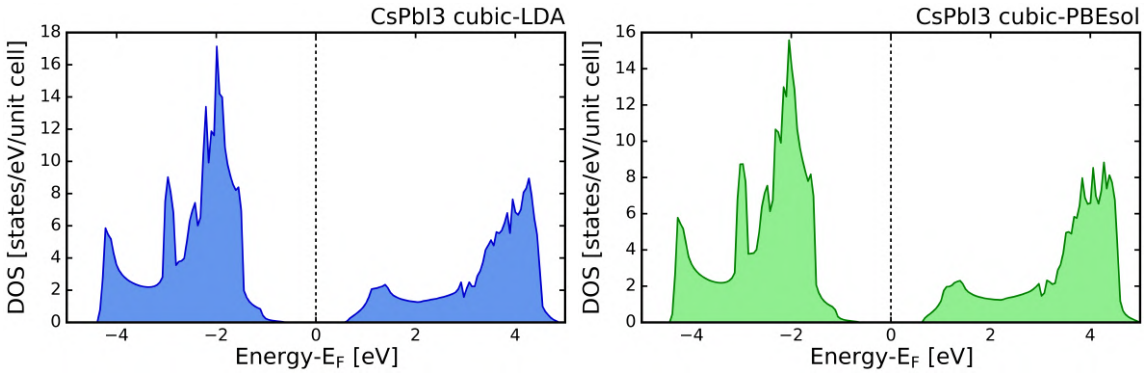

Bandgap: LDA $\rightarrow$ 1.235 eV | PBEsol $\rightarrow$ 1.257 eV

$$m^*_{\mathrm{VBM}} : \mathrm{LDA} \rightarrow \begin{bmatrix} -0.17 & 0 & 0 \\ 0 & -0.17 & 0 \\ 0 & 0 & -0.17 \end{bmatrix} \quad \mathrm{PBEsol} \rightarrow \begin{bmatrix} -0.17 & 0 & 0 \\ 0 & -0.17 & 0 \\ 0 & 0 & -0.17 \end{bmatrix}$$

$$m^*_{\mathrm{CBM}} : \mathrm{LDA} \rightarrow \begin{bmatrix} 0.45 & 0 & 0 \\ 0 & 0.08 & 0 \\ 0 & 0 & 0.49 \end{bmatrix} \quad \mathrm{PBEsol} \rightarrow \begin{bmatrix} 0.72 & 0.01 & -0.26 \\ 0.01 & 0.15 & -0.04 \\ -0.26 & -0.04 & 0.51 \end{bmatrix}$$

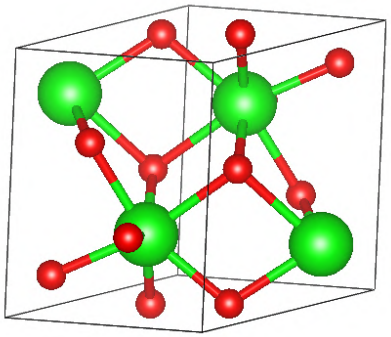

ZrO_2

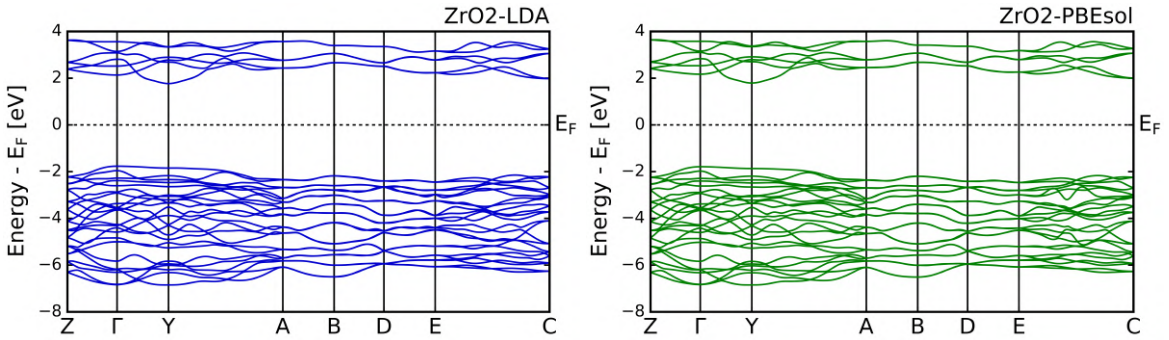

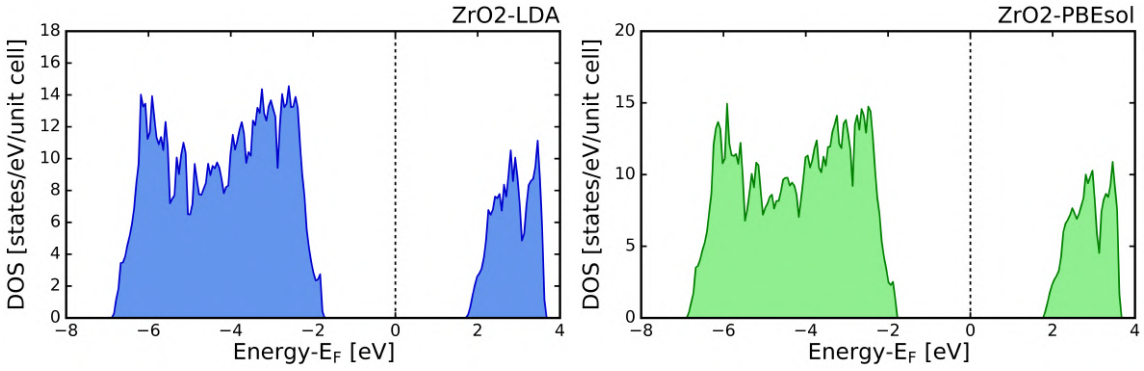

Bandgap: LDA $\rightarrow$ 3.530 eV | PBEsol $\rightarrow$ 3.574 eV

$$m^*_{\mathrm{VBM}} : \mathrm{LDA} \rightarrow \begin{bmatrix} -7.87 & 0.42 & -1.46 \\ 0.42 & -1.89 & 0.58 \\ -1.46 & 0.58 & -2.22 \end{bmatrix} \quad \mathrm{PBEsol} \rightarrow \begin{bmatrix} -7.72 & 1.05 & -1.71 \\ 1.05 & -1.85 & 0.05 \\ -1.71 & 0.05 & -2.32 \end{bmatrix}$$

$$m^*_{\mathrm{CBM}} : \mathrm{LDA} \rightarrow \begin{bmatrix} 1.01 & 0 & -0.98 \\ 0 & 0.89 & -0.05 \\ -0.98 & -0.05 & 3.49 \end{bmatrix} \quad \mathrm{PBEsol} \rightarrow \begin{bmatrix} 0.94 & -0.01 & -0.76 \\ -0.01 & 0.88 & -0.03 \\ -0.76 & -0.03 & 2.80 \end{bmatrix}$$

Chapter 6

Discussion

6.1 Electronic Bandstructure

The electronic band structure describes how electrons are distributed along a specific path in reciprocal space. It is crucial to analyze the behaviour of both the tightly bound electrons in the valence band and the free-to-move electrons in the conduction band.

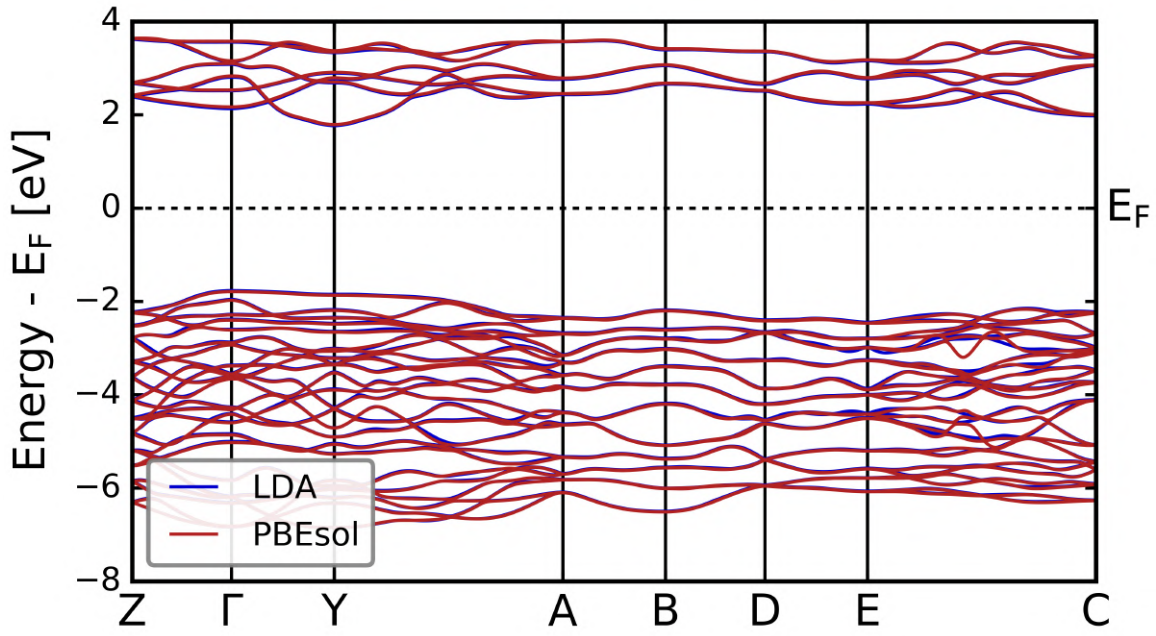

Figure 6.1: Electronic bandstructure plots of ZrO_2 calculated using LDA and PBEsol XC-functionals

Generally, it can be observed from the results section (5) that the bandstructure plots computed using LDA and GGA XC-functionals overlap well because the level of approximation is similar. Fig. (6.1) provides a better visualization of this observation with LDA and PBEsol plots of ZrO_2 overlaid.

In the case of $BaSnO_3$, results can be compared to more sophisticated hybrid functionals. Fig. 2.1 shows a combined plot of calculations for all the functionals used, aligned with respect to the VBM. Therefore, the valence bands are well-aligned, unlike the conduction bands. Fig. 2.1 indicates the opening of low-energy bands clearly. Both hybrid functional cases exhibit a large band opening, with PBE0 XC-functional showing a considerably greater effect than HSE06. This observation is consistent with the difference in bandgap values, indicating that PBE0 has the most significant band-opening effect. The results show an increase of 316% relative to LDA and 27% relative to HSE. Further analysis will determine which functional is more accurate in experiments. This observation is consistent with the literature, which has documented that hybrid functionals perform well in this scenario.

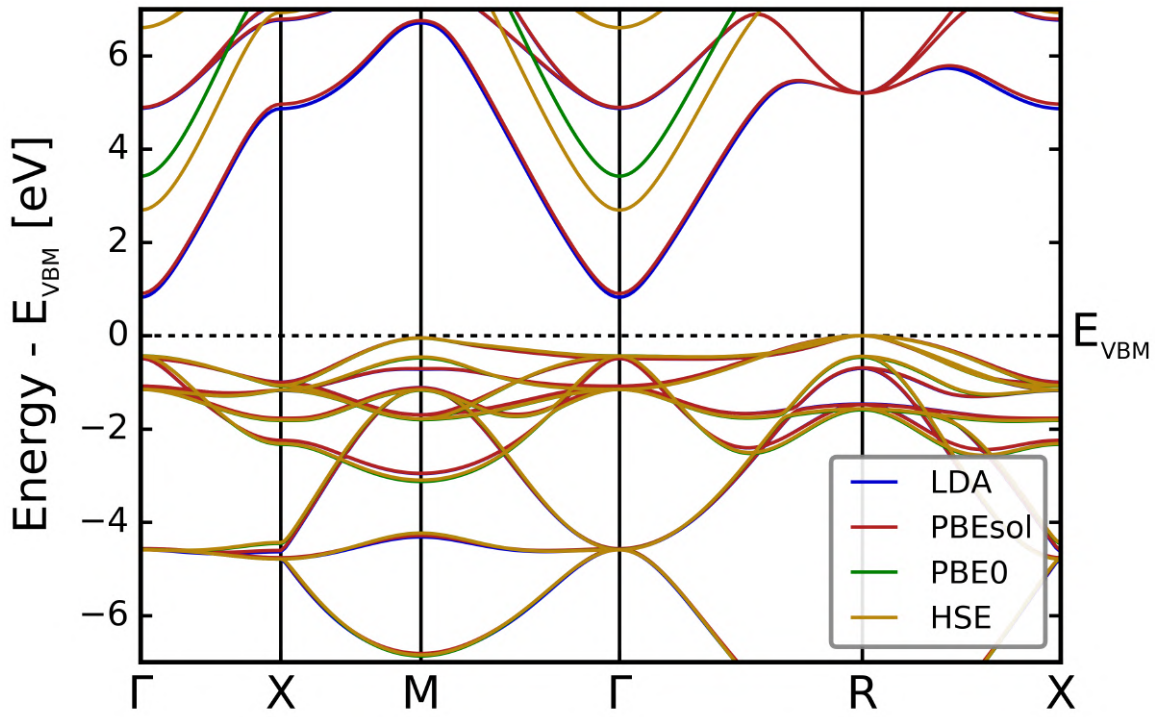

Figure 6.2: Electronic bandstructure plots of $BaSnO_3$ calculated using LDA, PBEsol, PBE0 and HSE06 XC-functionals

6.2 Electronic Density of States

The electronic density of states (DOS) is crucial for visualising the number of bands corresponding to a specific energy level. This plot also provides a clear visualisation of the bandgap in the system. The results show distinct overall behaviour; the valence band peaks near the band edge and decreases as the energy increases. On the other hand, the conduction band either has a peak near the Fermi level (in cases of high degeneracy) or is evenly distributed.

Similar to our analysis of the electronic band structure, Fig. (6.3) shows a plot for ZrO_2 using LDA and PBEsol XC-functionals. This plot confirms our previous observation that the LDA and GGA functionals produce similar band structures.

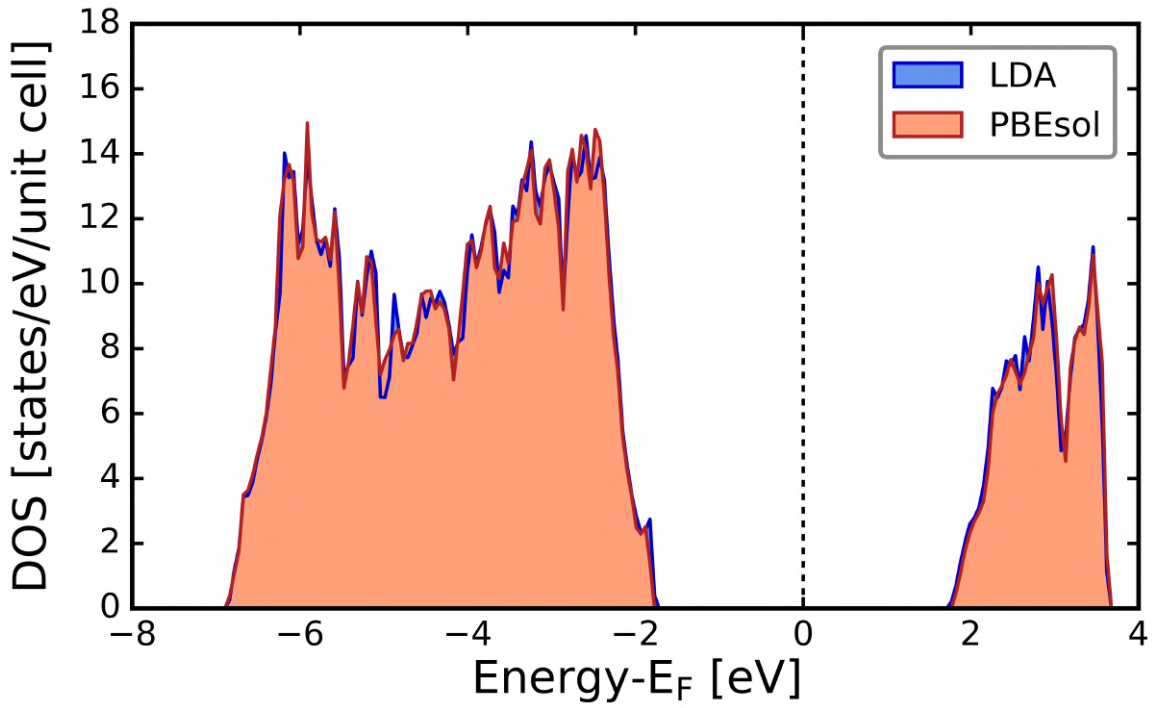

Figure 6.3: Electronic density of states of ZrO_2 using LDA and PBEsol XC-functionals

Fig. (6.4) shows the differences in computation using hybrids, which is significantly different from the LDA and GGA functionals. Additionally, the plot clearly displays a pronounced band opening. However, it is also possible to observe a shift in DOS peaks, they are not well represented as the bands are aligned with respect to the Fermi energy of the system.

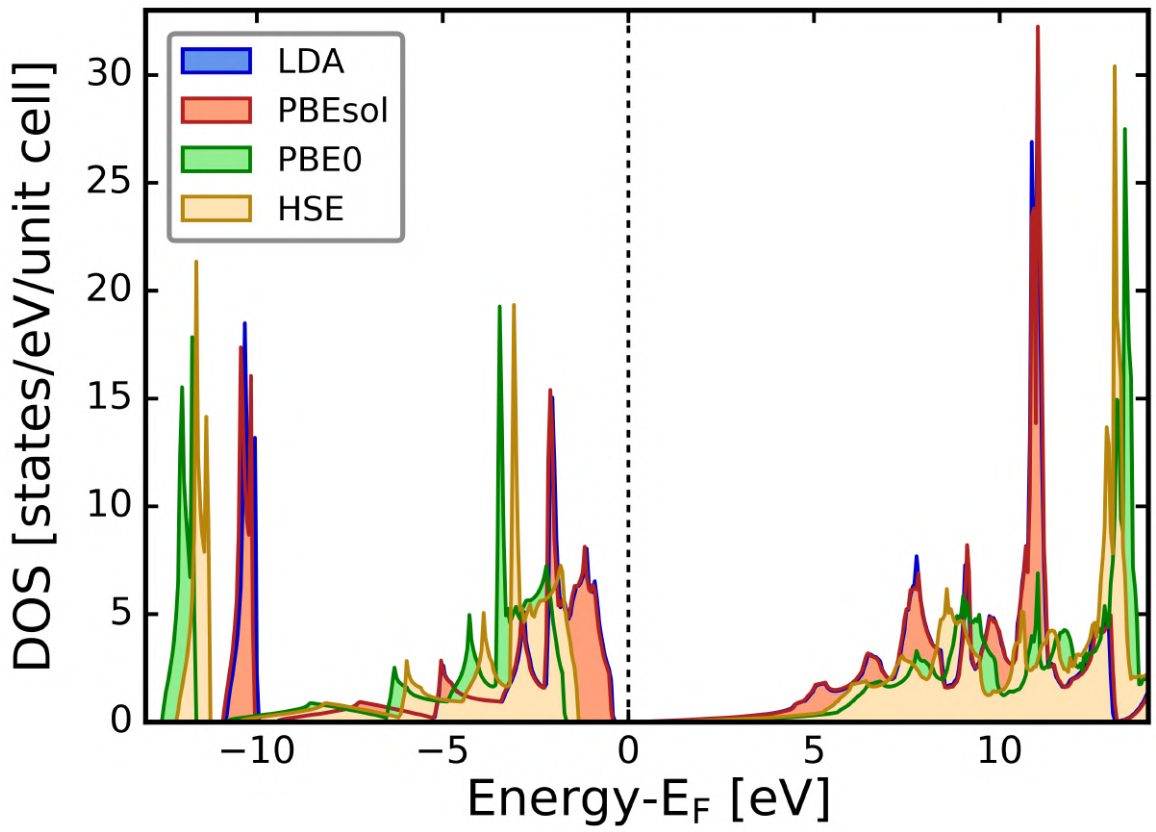

Figure 6.4: Electronic density of states of $BaSnO_3$ using LDA, PBEsol, PBE0 and HSE06 XC-functionals

6.3 Bandgap

The bandgap is one of the most widely studied and crucial properties for our systems of interest, as it determines electrical behaviour and, thus, the application of these materials. Electron mobility, optical absorption, and emission spectra are characteristic properties highly influenced by the bandgap. Although the values enlisted in the results section (5) provide a decent idea of the difference between various computations, we refer to Fig. (6.5) for better visualisation, showing a bar plot of the bandgap values calculated. Once again, the values for the LDA and GGA approximations are very similar, but both undermine the band gap compared to the Hybrids.

For the case of $BaSnO_3$, a quick comparison to experimental results (bandgap $\approx$ 2.7-3.4 eV) shows that the HSE06 functional is more 'accurate' but still underestimates, whereas PBE0 overshoots.

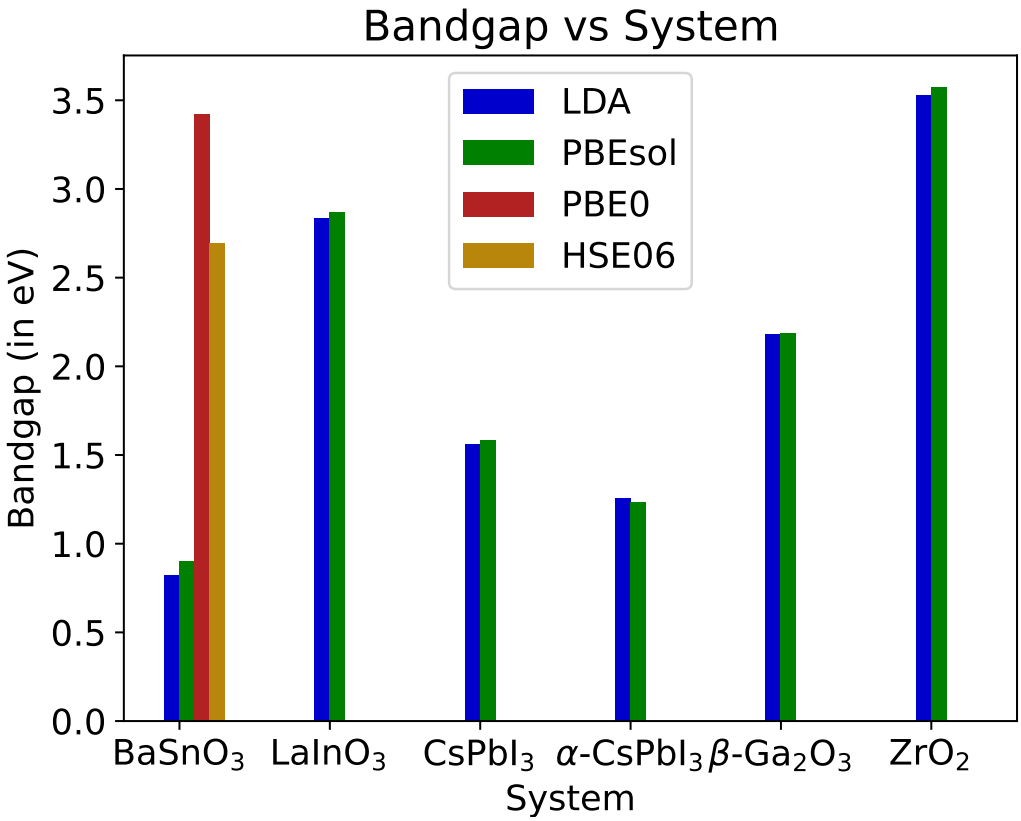

Figure 6.5: Comparison of the electronic bandgap of different materials based on different XC-functionals used

6.4 Effective masses

In the case of perovskites, it is important to describe the anisotropy of the crystal, which provides valuable insights into the electronic and transport properties of the material. Since the effective mass is a virtue of the band structure, we generate the effective masses at the band extremes by:

$$m^*_{\mathrm{VBM/CBM}}(k) = [\nabla_k \nabla_k^T \epsilon_{\mathrm{VBM/CBM}}(k)]^{-1} \tag{6.1}$$

From the results (5), we obtain the full effective mass tensors for all functionals. We opt for component-wise comparisons to observe how the use of a particular functional affects the value along a particular direction. Effective masses essentially quantify the curvature of a band. Therefore, a higher effective mass value corresponds to a more curved band structure. The effective masses are calculated on band extremes and can correspond to different k-points for the valence and conduction bands. Fig. (6.6)

shows the CBM of ZrO_2 calculated at the Y point. It is evident that the bands have very similar curvature, which is consistent as the effective mass tensors are also very similar. Similarly, Fig. (6.7) shows the enlarged band structure showing the VBM of the same material. The system has an indirect bandgap with VBM at Γ point. Again, the plots are very similar to each other, which is consistent with the values given in the results section.

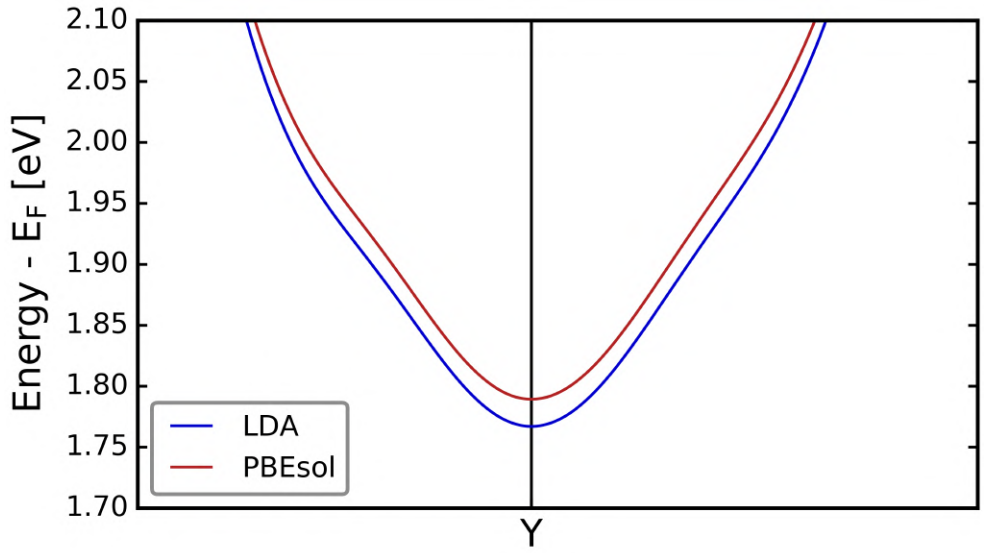

Figure 6.6: Zoomed bandstructure of ZrO_2 showing the CBM at Y≡($\frac{1}{2}$,0,0) point

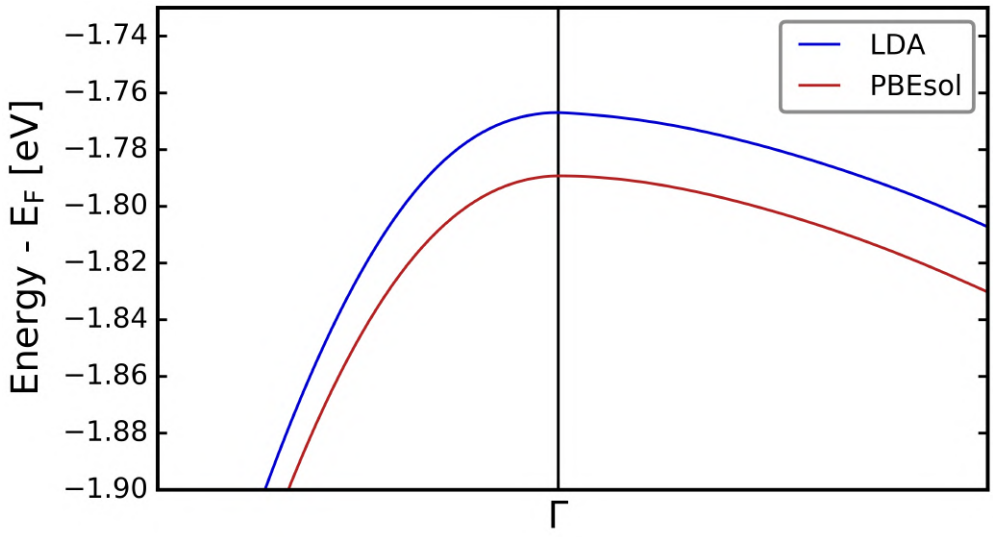

Figure 6.7: Zoomed bandstructure of ZrO_2 showing the VBM at Γ point

Chapter 7

Conclusion

This study has been focused on performing and accumulating highly precise electronic structure calculations on perovskites and metal-oxide materials. Our motive was to bridge the gap in the community created by the absence of highly precise groundstate DFT calculations. We choose the LAPW+lo method for this purpose as it is often considered the gold standard of DFT. The database 'Benchmark DFT groundstate calculations' is available on NOMAD.

The primary challenge encountered in the project was selecting suitable basis functions and converged parameters to effectively model the wave function. We developed a comprehensive workflow that can be easily adapted and reused for all calculations, as we had to re-perform convergence tests and preliminary calculations multiple times.

Having computed groundstate DFT calculations, we analysed many band properties of the system. We observed that the electronic bandstructure, density of states, and bandgap follow a general trend, and LDA and GGA XC-functionals gave very coherent results. Meanwhile, the hybrid functionals generated higher bandgaps and shifts in the overall band structure. It can be concluded that hybrid functionals act as shift operators on the LDA, GGA parameterized band structure. Moreover, the results of effective mass tensors infer that higher energy bands are also coherent with this scissor shift operation, as the component-wise comparison of effective masses yields very little deviation. Hence, the band curvature for these different functionals is similar.

Since we compute well-documented observables, comparison to experimental calculations is natural. However, such comparisons are not within the scope of this study as we do not consider effects such as electron-phonon interactions, spin-orbit coupling, optical electron-hole effects or quasiparticle energies, which are essential for systems with heavy p-orbital contributions.

Future directions: We have analysed six materials in this project. However, we have created a comprehensive workflow to incorporate more materials. In the future, this project will be extended to include more high-throughput calculations using additional materials, functionals, and techniques. The formalism can eventually be extended to include excited state calculations, electron-phonon effects and spin-orbit coupling, resulting in a database focused on 'accurate' calculations.

Bibliography

[1] Andris Gulans, Stefan Kontur, Christian Meisenbichler, Dmitrii Nabok, Pasquale Pavone, Santiago Rigamonti, Stephan Sagmeister, Ute Werner, and Claudia Draxl. exciting: a full-potential all-electron package implementing density-functional theory and many-body perturbation theory. *Journal of Physics: Condensed Matter*, 26(36):363202, aug 2014.

[2] Claudia Draxl and Matthias Scheffler. The NOMAD laboratory: from data sharing to artificial intelligence. *JPhys Mater.*, 2(3):036001, July 2019.

[3] J. C. Slater and G. F. Koster. Simplified lcao method for the periodic potential problem. *Phys. Rev.*, 94:1498–1524, Jun 1954.

[4] Douglas Rayner Hartree and W. Hartree. Self-consistent field, with exchange, for beryllium. *Proceedings of the Royal Society of London. Series A - Mathematical and Physical Sciences*, 150(869):9–33, 1935.

[5] P. Hohenberg and W. Kohn. Inhomogeneous electron gas. *Phys. Rev.*, 136:B864–B871, Nov 1964.

[6] Kieron Burke. Perspective on density functional theory. *The Journal of Chemical Physics*, 136(15):150901, 04 2012.

[7] R. O. Jones. Density functional theory: Its origins, rise to prominence, and future. *Rev. Mod. Phys.*, 87:897–923, Aug 2015.

[8] Anubhav Jain, Shyue Ping Ong, Geoffroy Hautier, Wei Chen, William Davidson Richards, Stephen Dacek, Shreyas Cholia, Dan Gunter, David Skinner, Gerbrand Ceder, and Kristin A. Persson. Commentary: The Materials Project: A materials genome approach to accelerating materials innovation. *APL Materials*, 1(1):011002, 07 2013.

[9] Colin R Groom, Ian J Bruno, Matthew P Lightfoot, and Suzanna C Ward. The cambridge structural database. *Acta Crystallogr. B Struct. Sci. Cryst. Eng. Mater.*, 72(Pt 2):171–179, April 2016.

[10] Peter Linstrom. NIST chemistry WebBook, NIST standard reference database 69, 1997.

[11] Manuel Richter, Seo-Jin Kim, Klaus Koepernik, Helge Rosner, and Arnulf Möbius. Accuracy and precision in electronic structure computation: Wien2k and fplo. *Computation*, 10:28, 02 2022.

[12] Cecilia Vona, Dmitrii Nabok, and Claudia Draxl. Electronic structure of (organic-)inorganic metal halide perovskites: The dilemma of choosing the right functional. *Adv. Theory Simul.*, 5(1):2100496, January 2022.

[13] Roger H. Mitchell, Mark D. Welch, and Anton R. Chakhmouradian. Nomenclature of the perovskite supergroup: A hierarchical system of classification based on crystal structure and composition. *Mineralogical Magazine*, 81(3):411–461, 06 2017.

[14] Quinten A. Akkerman and Liberato Manna. What defines a halide perovskite? *ACS Energy Letters*, 5(2):604–610, Feb 2020.

[15] V. M. Goldschmidt. Die gesetze der krystallochemie. *Naturwissenschaften*, 14(21):477–485, May 1926.

[16] W. Travis, E. N. K. Glover, H. Bronstein, D. O. Scanlon, and R. G. Palgrave. On the application of the tolerance factor to inorganic and hybrid halide perovskites: a revised system. *Chem. Sci.*, 7:4548–4556, 2016.

[17] Christopher J. Bartel, Christopher Sutton, Bryan R. Goldsmith, Runhai Ouyang, Charles B. Musgrave, Luca M. Ghiringhelli, and Matthias Scheffler. New tolerance factor to predict the stability of perovskite oxides and halides. *Science Advances*, 5(2):eaav0693, 2019.

[18] The role of interfaces on the photoluminescence of orthorhombic CsPbI3 thin films. *Advanced Functional Materials*, 2018.

[19] In Chung, Jung-Hwan Song, Jino Im, John Androulakis, Christos D Malliakas, Hao Li, Arthur J Freeman, John T Kenney, and Mercouri G Kanatzidis. CsSnI3: Semiconductor or metal? high electrical conductivity and strong near-infrared photoluminescence from a single material. high hole mobility and phase-transitions. *J. Am. Chem. Soc.*, 134(20):8579–8587, May 2012.

[20] Eman Abdul Rahman Assirey. Perovskite synthesis, properties and their related biochemical and industrial application. *Saudi Pharmaceutical Journal*, 27(6):817–829, 2019.

[21] Hyun Suk Jung and Nam-Gyu Park. Perovskite solar cells: from materials to devices. *Small*, 11(1):10–25, January 2015.

[22] Iness R Benmessaoud, Anne-Laure Mahul-Mellier, Endre Horváth, Bohumil Maco, Massimo Spina, Hilal A Lashuel, and Làszló Forró. Health hazards of methylammonium lead iodide based perovskites: cytotoxicity studies. *Toxicol. Res. (Camb.)*, 5(2):407–419, 2016.

[23] Junming Li, Hai-Lei Cao, Wen-Bin Jiao, Qiong Wang, Mingdeng Wei, Irene Cantone, Jian Lü, and Antonio Abate. Biological impact of lead from halide perovskites reveals the risk of introducing a safe threshold. *Nature Communications*, 11(1):310, Jan 2020.

[24] Philip Schulz, David Cahen, and Antoine Kahn. Halide perovskites: Is it all about the interfaces? *Chem. Rev.*, 119(5):3349–3417, March 2019.

[25] Andreas Stadler. Transparent conducting oxides—an up-to-date overview. *Materials*, 5(4):661–683, 2012.

[26] J. Y. Tsao, S. Chowdhury, M. A. Hollis, D. Jena, N. M. Johnson, K. A. Jones, R. J. Kaplar, S. Rajan, C. G. Van de Walle, E. Bellotti, C. L. Chua, R. Collazo, M. E. Coltrin, J. A. Cooper, K. R. Evans, S. Graham, T. A. Grotjohn, E. R. Heller, M. Higashiwaki, M. S. Islam, P. W. Juodawlkis, M. A. Khan, A. D. Koehler, J. H. Leach, U. K. Mishra, R. J. Nemanich, R. C. N. Pilawa-Podgurski, J. B. Shealy, Z. Sitar, M. J. Tadjer, A. F. Witulski, M. Wraback, and J. A. Simmons. Ultrawide-bandgap semiconductors: Research opportunities and challenges. *Advanced Electronic Materials*, 4(1):1600501, 2018.

[27] Hengxin Tan, Haitao Liu, Yuanchang Li, Wenhui Duan, and Shengbai Zhang. Understanding the origin of bandgap problem in transition and post-transition metal oxides. *The Journal of Chemical Physics*, 151(12):124703, 09 2019.

[28] Rustum Roy, VG Hill, and EF Osborn. Polymorphism of ga2o3 and the system ga2o3—h2o. *Journal of the American Chemical Society*, 74(3):719–722, 1952.

[29] M Born and R Oppenheimer. Zur quantentheorie der molekeln. *Ann. Phys.*, 389(20):457–484, January 1927.

[30] W Kohn and L J Sham. Self-consistent equations including exchange and correlation effects. *Phys. Rev.*, 140(4A):A1133–A1138, November 1965.

[31] David Singh. Ground-state properties of lanthanum: Treatment of extended-core states. *Phys. Rev. B*, 43:6388–6392, Mar 1991.

[32] John P. Perdew and Karla Schmidt. Jacob's ladder of density functional approximations for the exchange-correlation energy. *AIP Conference Proceedings*, 577(1):1–20, 07 2001.

[33] Diola Bagayoko. Understanding density functional theory (DFT) and completing it in practice. *AIP Advances*, 4(12):127104, 12 2014.

[34] John P. Perdew, J. A. Chevary, S. H. Vosko, Koblar A. Jackson, Mark R. Pederson, D. J. Singh, and Carlos Fiolhais. Atoms, molecules, solids, and surfaces: Applications of the generalized gradient approximation for exchange and correlation. *Phys. Rev. B*, 46:6671–6687, Sep 1992.

[35] Axel D. Becke. Density-functional thermochemistry. III. The role of exact exchange. , 98(7):5648–5652, April 1993.

[36] J P Perdew, K Burke, and M Ernzerhof. Generalized gradient approximation made simple. *Phys. Rev. Lett.*, 77(18):3865–3868, October 1996.

[37] John P. Perdew, Matthias Ernzerhof, and Kieron Burke. Rationale for mixing exact exchange with density functional approximations. *The Journal of Chemical Physics*, 105(22):9982–9985, 12 1996.

[38] Jochen Heyd, Gustavo E. Scuseria, and Matthias Ernzerhof. Hybrid functionals based on a screened Coulomb potential. *The Journal of Chemical Physics*, 118(18):8207–8215, 04 2003.

[39] Kevin F. Garrity, Joseph W. Bennett, Karin M. Rabe, and David Vanderbilt. Pseudopotentials for high-throughput dft calculations. *Computational Materials Science*, 81:446–452, 2014.

[40] P. E. Blöchl. Projector augmented-wave method. *Phys. Rev. B*, 50:17953–17979, Dec 1994.

[41] E Sjöstedt, L Nordström, and D.J Singh. An alternative way of linearizing the augmented plane-wave method. *Solid State Communications*, 114(1):15–20, 2000.

[42] O. Krogh Andersen. Linear methods in band theory. *Phys. Rev. B*, 12:3060–3083, Oct 1975.

[43] Andris Gulans, Anton Kozhevnikov, and Claudia Draxl. Microhartree precision in density functional theory calculations. *Phys. Rev. B*, 97:161105, Apr 2018.

[44] Wahyu Setyawan and Stefano Curtarolo. High-throughput electronic band structure calculations: Challenges and tools. *Computational Materials Science*, 49(2):299–312, 2010.

[45] John P. Perdew and Yue Wang. Accurate and simple analytic representation of the electron-gas correlation energy. *Phys. Rev. B*, 45:13244–13249, Jun 1992.

[46] John P Perdew, Adrienn Ruzsinszky, Gábor I Csonka, Oleg A Vydrov, Gustavo E Scuseria, Lucian A Constantin, Xiaolan Zhou, and Kieron Burke. Restoring the density-gradient expansion for exchange in solids and surfaces. *Phys. Rev. Lett.*, 100(13):136406, April 2008.

[47] Carlo Adamo and Vincenzo Barone. Toward reliable density functional methods without adjustable parameters: The PBE0 model. *The Journal of Chemical Physics*, 110(13):6158–6170, 04 1999.

[48] Wahyu Setyawan and Stefano Curtarolo. High-throughput electronic band structure calculations: Challenges and tools. *Computational Materials Science*, 49(2):299–312, 2010.